


## REVIEW

[View Article Online](#)  
[View Journal](#) | [View Issue](#)Cite this: *Nanoscale*, 2023, **15**, 11777

# Recent progress in the synthesis of transition metal nitride catalysts and their applications in electrocatalysis

Zheng-Gang Yang, Hui-Min Xu, Ting-Yu Shuai, Qi-Ni Zhan, Zhi-Jie Zhang, Ke Huang, Chunlong Dai and Gao-Ren Li \*

Transition metal nitrides (TMNs) have become excellent substitutes for precious metals such as Pt and Ir in the field of electrocatalysis because of their excellent electrocatalytic performance, high conductivity, good corrosion resistance and stability. As we all know, the commonly utilized carbon-based materials corrode easily during electrocatalysis, which will lead to catalyst falling off and agglomeration. Compared with carbon-based materials, TMNs have stronger corrosion resistance and higher stability. In the metal nitrides, a variety of chemical bonds (metal bond, ionic bond and covalent bond) coexist, among which the ionic bond between metal atoms and nitrogen atoms can make the d-band shrink and narrow, which leads to TMNs having characteristics similar to precious metals in the electrocatalytic process; thus, they can be used as a substitute for precious metal catalysts. In this paper, the synthesis method and catalytic principle of transition metal nitrides and their applications in the fields of hydrogen evolution reaction (HER), oxygen evolution reaction (OER) and oxygen reduction reaction (ORR) are discussed, and the shortcomings of TMNs as a catalyst, the challenges faced in catalyst research and the developments and prospects for the future are pointed out.

Received 7th April 2023,  
Accepted 5th June 2023

DOI: 10.1039/d3nr01607b

[rsc.li/nanoscale](https://rsc.li/nanoscale)

## 1. Introduction

With the intensification of the global greenhouse effect, developing new energy sources while reducing the use of chemical energy has become an inevitable trend. The development of hydrogen energy and fuel cells in practice is one of the main research directions. The energy density of hydrogen (142 MJ kg<sup>-1</sup>) is much higher than that of gasoline (44 MJ kg<sup>-1</sup>),<sup>1</sup> and the combustion product of hydrogen is water, so hydrogen is known as the cleanest energy in the 21st century. At present, the main sources of hydrogen production are coal and natural gas, but there are some problems in the process of hydrogen production, such as the generation of many by-products, the emission of carbon dioxide and the low purity of hydrogen. A very promising hydrogen production technology, hydrogen generation from water electrolysis, can produce high-purity hydrogen. However, the oxygen evolution reaction (OER) at the anode and the hydrogen evolution reaction (HER) at the cathode show large overpotentials, which seriously restrict the large-scale application of hydrogen production from water electrolysis.<sup>2</sup> As we all know, the OER is a four-electron reaction,

which is extremely slow in electrocatalytic water decomposition. Achieving efficient OER and HER with low overpotentials has become a major challenge. Choosing a suitable catalyst can effectively reduce the overpotentials of anode and cathode to increase the catalytic rate. Similarly, the cathode half-reaction oxygen reduction reaction (ORR) is the main limiting factor for fuel cell performance.<sup>3</sup> At present, most of OER, HER and ORR catalysts on the market are precious metals such as Pt and Ir. Although precious metals are effective catalysts for the different catalytic reactions above, their natural scarcity and high cost have brought great obstacles to large-scale production.<sup>4</sup> Therefore, the development of low-cost and high-performance electrocatalysts has become the focus of current research.

At present, various catalysts such as transition metal sulfides, borides, carbides, and nitrides have been developed around transition metals. Metal sulfides have poor conductivity and are prone to expansion during use. The synthesis of metal borides is difficult, the poor corrosion resistance of carbides means easy fall off, and the poor conductivity of metal oxides limits their applications. However, the transition metal nitride (TMN) catalyst has high stability, good corrosion resistance and excellent conductivity. The d-band contraction makes its structure similar to that of noble metals, which is promising as a non-noble metal catalyst.<sup>5</sup> In this review, some

College of Materials Science and Engineering, Sichuan University, Chengdu 610065, China. E-mail: [ligaoren@scu.edu.cn](mailto:ligaoren@scu.edu.cn)

commonly used synthesis methods of transition metal nitrides and the reasons for their excellent catalytic performance are highlighted. The applications of transition metal nitrides in the fields of HER, OER and ORR are summarized, and the shortcomings of transition metal nitrides and the aspects that can be improved are proposed.

## 2. Mechanism of high electrocatalytic performance of transition metal nitrides

In the transition metal nitrides, the nitrogen atom is in the gap of the metal lattice, and the insertion of a nitrogen atom will change the structure of the parent metal. The above effect on the catalytic activity can be explained by the modification of the d-band and the direction and number of charge transfer.<sup>7,8</sup> The band structure of transition metal nitrides (Fig. 1a) is like that of noble metals (fcc) in shape and relative order,<sup>10</sup> which may be the reason for their similar catalytic properties. For transition metals, below the Fermi level, the filled state of the d-band becomes narrower after the formation of TMNs, making its electronic structure like that of noble metals. Above the Fermi level, the unfilled state of the metal in TMNs will become wider, so that the empty energy level density is greater than that of the parent metal. The d-band near the Fermi level is not occupied enough, and the transfer ability of d electrons from the nitride surface to the adsorbate is reduced. Therefore, the expansion of the d-band unfilled

state makes the catalyst a better electron acceptor, which is beneficial for improving the catalytic performance. Especially for the reaction of transferring the bonding electrons to the unfilled orbits of the metal substrate, TMNs have better activity than the parent metal and noble metal.<sup>5</sup> As shown in Fig. 1b, Chen *et al.* found that NiMo alloy has a pre-edge feature at 20 004 eV,<sup>6</sup> which indicates the presence of d-band holes. Compared with NiMo alloy, the white line of Mo K-edges of NiMoN<sub>x</sub> changes significantly. The formation of metal–nitrogen bonds will change the density of states of the parent metal unfilled d-bands. The lower d-band occupation defect of Mo makes NiMoN<sub>x</sub> have a stronger electron-donating ability. In addition, another electronic property of TMNs is the direction and number of charge transfer. In TMNs, the charge is transferred from the metal atom to the nitrogen atom. The amount of charge transfer determines the ionicity of the TMN, and the ionicity of TMNs formed by the parent metal from VIB to IVB group will gradually increase because the electronegativity of the parent metal decreases.<sup>7</sup> In addition, transition metal nitrides have high stability due to their salt rock-type (NaCl-type) structure, where each metal atom (or nitrogen atom) is coordinated with six nitrogen atoms (or metal atoms), which is an octahedral coordination, as shown in Fig. 1c and d.<sup>7,9</sup>

The second transition metal-doped TMNs have a wide range of applications. Most of their structures are layered structures. The second transition metal occupies the octahedral gap between the layers, as shown in Fig. 1e.<sup>11</sup> The synergistic effect between metals can enhance the catalytic activity. The electronic structure and electron density of the bi-metallic nitride formed by the introduction of the second

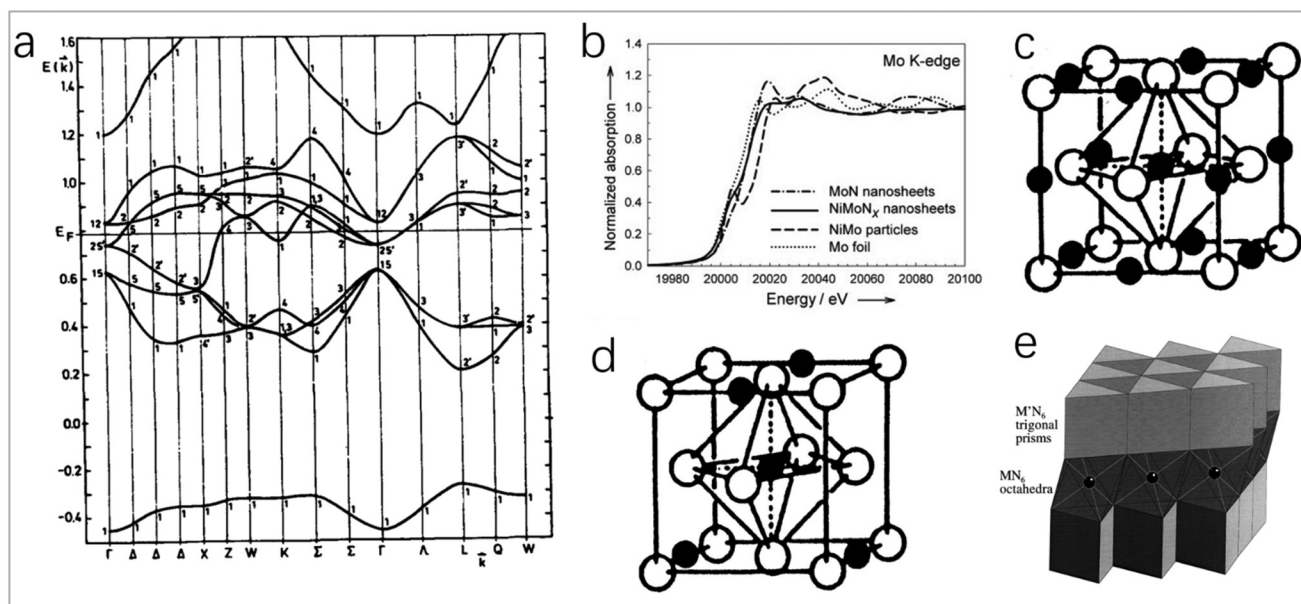


**Fig. 1** (a) Band structure of TiN<sub>1.0</sub> calculated using the APW method.<sup>10</sup> Copyright 1995, ScienceDirect; (b) Mo K-edges from NiMo nanoparticles and NiMoN<sub>x</sub> nanosheets as well as Ni and Mo foils.<sup>6</sup> Copyright 2012, Wiley-VCH; (c and d) typical structures of transition metal carbides and nitrides.<sup>7</sup> Copyright 1996, American Chemical Society; (e) most prominent stacking variant of MM'N<sub>2</sub> nitrides (e.g., FeWN<sub>2</sub>), with M' = Mo, W in trigonal prismatic coordination by nitrogen atoms, and the transition metal M (e.g., Mn, Fe, Co, Ni) coordinated octahedrally.<sup>11</sup> Copyright 1998, American Chemical Society.

metal will change, which will reduce the free energy of hydrogen adsorption and increase the adsorption energy of hydroxide, and accordingly will improve the HER and OER catalytic activity of the catalyst. Doping secondary metals with rich d electrons into TMNs will increase d electrons of the catalyst, which can improve the ORR catalytic performance.<sup>82,93,141</sup> The introduction of another metal atom will enhance the chemical stability and conductivity of TMNs, so bimetallic nitrides often have higher catalytic activity and stability than single-metal nitrides.<sup>12,13</sup> In addition, in the bimetallic system, the transfer of electrons between two different groups will cause changes in the electronic band structure, and there will be ligand effects; when the surface atoms are compressed or expanded, there will be strain effects in TMNs. The above ligand effects and strain effects will affect the adsorption state of the intermediate on the catalysts and further affect the catalytic activity.<sup>124</sup>

The coupling of carbon materials with TMNs can increase active sites and enhance charge transfer, so that TMNs/carbon materials have higher activity and conductivity than single-metal nitrides and bimetallic nitrides, and enhance stability to a certain extent. The doping of carbon can enhance the adsorption of H\*, improve the stability of O\* intermediates, and increase adsorption energy of active sites to oxygen-containing intermediates, so that the catalyst has high HER, OER and ORR catalytic performance.<sup>45,129–131</sup> At present, the commonly used carbon materials include graphene, carbon nanotubes, graphite arrays, *etc.*, and they have good electrical conductivity and large active area. Carbon nitride is a nitrogen-doped carbon nanotube array with long life, high durability, and versatility. It is also used in electrocatalysis in combination with metal nitrides.<sup>142</sup> In addition, some design strategies can improve the catalytic activity and stability of TMNs, such as synergistic metal-support interactive TMNs catalysts, heterogeneous interface TMNs catalysts, *etc.*<sup>14</sup>

### 3. The main synthesis methods of transition metal nitrides

As a new type of non-precious metal catalyst, the TMNs can be divided into single-metal nitrides, bimetallic nitrides and composite metal nitrides. The synthesis methods of various TMNs include the direct ammoniation of precursors, solvothermal method, impregnation adsorption method, metal-organic framework thermal decomposition, chemical vapor deposition, *etc.* The different synthesis methods may lead to various catalytic activities of similar catalysts, so the synthesis method is extremely important for the preparation of catalyst.

#### 3.1 Direct ammoniation of precursors

The direct ammoniation of precursors is a common synthesis method for the preparation of TMN nanofibers or micro/nanotubes. The general steps are listed as follows: (i) synthesis of composite precursors with desired morphology; (ii) metal nitrides can be prepared by ammoniating the precursors in

ammonia to remove organic components.<sup>15</sup> Chen *et al.* directly ammoniated the precursor of Co-based zeolite imidazolate framework (ZIF-67) in NH<sub>3</sub> flowing gas.<sup>16</sup> In this process, Co ions were dissociated from ZIF-67 and reacted with NH<sub>3</sub> to form Co<sub>5.47</sub>N nanoparticles. ZIF-67 is a nitrogen-doped framework assembled using cobalt nitrate as metal salt and dimethylimidazole as linker, and it has high stability and large surface area.<sup>132</sup> The organic ligand was decomposed *in situ* and then carbonized into nitrogen-doped porous carbon, which forms a three-dimensional porous structure around Co<sub>5.47</sub>N nanoparticles. The above synthesis process is shown in Fig. 2a. Shin *et al.* reported that the dried titanate nanofibers were placed in a flow furnace, and flowing NH<sub>3</sub> was introduced. The temperature was gradually increased to 800 °C and then annealing for 2 hours took place. Finally the obtained dark powder was treated to obtain spherical TiN nanoparticles.<sup>17</sup> Li *et al.* used Ti(OBu)<sub>4</sub>/PVP composite nanofibers (Fig. 2b) as the precursor to prepare a TiN sample.<sup>18</sup> After ammoniating at 900 °C, the obtained TiN exhibited continuous and uniform nanofibers (Fig. 2c). Compared with that of the precursor, the surface of TiN nanofibers was relatively rough because they were composed of TiN crystalline nanoparticles with a diameter of about 16 nm (Fig. 2d). In addition, Ni<sub>3</sub>FeN@C/NF could be obtained by soaking Ni<sub>3</sub>Fe-OH/NF in 0.1 M glucose for 24 hours and annealing at 400 °C for 2 hours in ammonia atmosphere.<sup>19</sup>

The regulation of temperature during the direct ammoniation synthesis process will affect the performance of the catalyst. Different temperatures during nitriding will give the catalyst different catalytic activity and stability. Yu *et al.* placed the precursor CoWO<sub>4</sub> nanoparticles at different temperatures (550 °C, 650 °C and 750 °C);<sup>20</sup> the ammonia flow rate was 100 sccm (standard cubic centimeter per minute), the heating rate was 5 °C min<sup>-1</sup>, and the Co<sub>4</sub>N-WN<sub>x</sub> (CWN-x) nanoparticle samples were prepared at different temperatures after holding for two hours (x is different temperature). The prepared CWN-750 sample had the smallest particle size (Fig. 2e–h), and the particle size was only 23 nm. As shown in Fig. 2i, the catalytic water-splitting test of Co<sub>4</sub>N-WN<sub>x</sub> nanoparticles showed that CWN-750 had the best hydrogen evolution catalytic performance (262.7 μmol g<sup>-1</sup> h<sup>-1</sup>) among all samples (Fig. 2j and k). Nitride materials with small particle size, uniform size distribution, uniform composition and high catalytic performance can be prepared by the direct ammoniation of the precursor. The key to this method is to find and synthesize the appropriate precursors.

#### 3.2 Solvothermal method

The solvothermal reaction is carried out at a certain temperature and pressure in water or organic solvent in a high-pressure reactor. It can be carried out at a lower temperature, which is due to the solvent dissipating the enthalpy of reaction and reducing the diffusion barrier between the reactants.<sup>21</sup> Wu *et al.* used Cu(NO<sub>3</sub>)<sub>2</sub>·3H<sub>2</sub>O to prepare Cu<sub>3</sub>N in primary amine (surfactant) and octadecene (ODE) (solvent).<sup>22</sup> The syn-



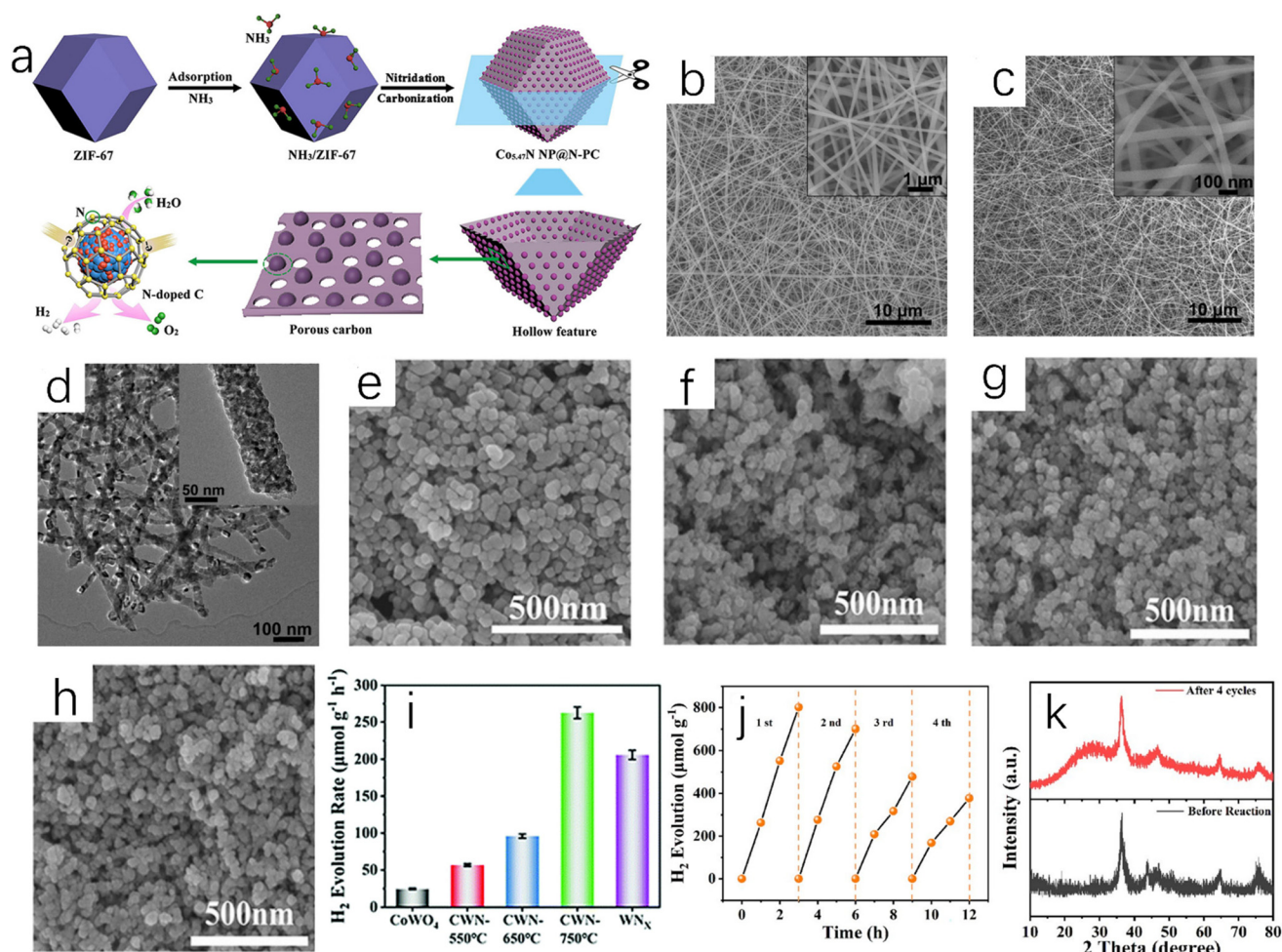
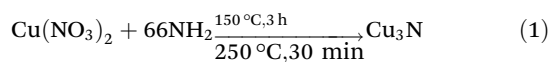


**Fig. 2** (a) A schematic diagram of the synthesis process of  $\text{Co}_{5.47}\text{N NP@N-PC}$ .<sup>16</sup> Copyright 2018, American Chemical Society; (b) SEM image of typical electrospun  $\text{Ti}(\text{OBu})_4/\text{PVP}$  composite nanofibers as TiN nanofiber precursors (inset: high-magnification SEM image); (c) SEM image of TiN nanofibers synthesized at 900 °C (inset: high-magnification SEM image); (d) TEM image of TiN nanofibers fabricated at 900 °C (inset: high-magnification TEM image).<sup>18</sup> Copyright 2011, Royal Society of Chemistry. SEM images of (e)  $\text{CoWO}_4$ , (f) CWN-550, (g) CWN-650 and (h) CWN-750; (i) ultra-sonic hydrogen production rate of  $\text{CoWO}_4$ , CWN-550, CWN-650, CWN-750,  $\text{WN}_x$  and  $\text{Co}_4\text{N}$ ; (j) cyclic tests of piezoelectric catalytic hydrogen production on CWN-750; (k) XRD patterns of CWN-750 samples before and after stability test.<sup>20</sup> Copyright 2022, Royal Society of Chemistry.

thesis reaction is shown in eqn (1), and the size of the product of  $\text{Cu}_3\text{N}$  can be controlled by changing the surfactant.



Deshmukh *et al.* mixed ethanol solution of  $\text{Cu}(\text{OAc})_2 \cdot \text{H}_2\text{O}$  with  $(\text{MeO})_3\text{Si}(\text{CH}_2)_3\text{NH}_2(\text{CH}_2)_2\text{NH}_2(\text{AEAPTS})$  to generate  $[\text{Cu}(\text{AEAPTS})_2]^{2+}$  metal complexes,<sup>23</sup> and then mixed them with  $\text{Si}(\text{OEt})_4$  under alkaline condition for sol-gel treatment. The products were calcined in the air to remove possible carbides or carbonitrides. The obtained  $\text{CuO@SiO}_2$  composites were then reacted with ammonia at 300 °C for 8 h to prepare  $\text{Cu}_3\text{N@SiO}_2$  nanocomposites (Fig. 3a). Besides ammonia, urea also can be used as a nitrogen source. The urea glass method proposed by Yuan *et al.* can synthesize ZrN nanoparticles at a medium temperature (800 °C) (Fig. 3b).<sup>24</sup> The urea glass method can inhibit the growth and aggregation of

grains and increase the active surface area of ZrN. Choi *et al.* synthesized nickel nitride (NiN) by the solvothermal method,<sup>25</sup> and then dried it under dynamic vacuum at 200 °C to prevent the final product from containing NiO crystals. During the synthesis of NiN, the nickel nitride precursor was heated to promote the formation of metal azide intermediates, and then continued to be heated up for more than four days (20 °C per day) to promote the decomposition of azides. The authors also synthesized iron nitrides and manganese nitrides using a similar synthesis method. The scanning electron microscope images of NiN and FeN are shown in Fig. 3c and d. These two products are composed of aggregate particles with a size of 100–500 nm, which are eventually arranged into aggregates of micron size. Fig. 3e shows the scanning electron microscope image of MnN, which is mainly composed of particles with a size of about 100 nm and a rod-like structure with a length of 150 nm.

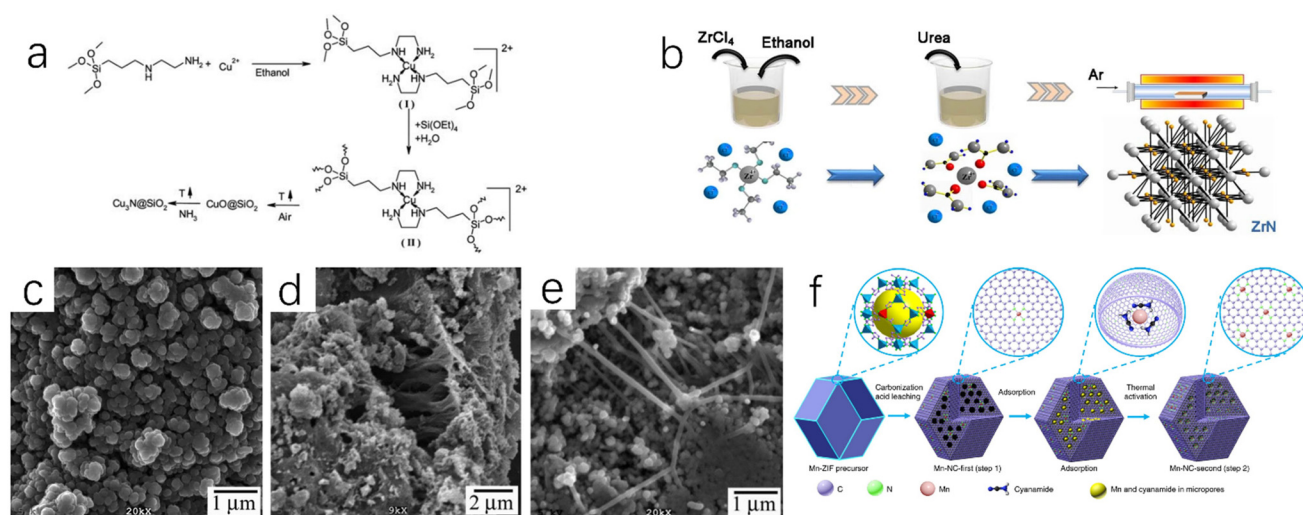


**Fig. 3** (a) Synthetic route of  $\text{Cu}_3\text{N}@ \text{SiO}_2$  nanocomposites by sol-gel method.<sup>23</sup> Copyright 2011, Royal Society of Chemistry; (b) synthetic route of ZnN NPS by urea glass method.<sup>24</sup> Copyright 2020, Springer Nature. SEM images of solvothermal products NiN (c), FeN (d), and MnN (e).<sup>25</sup> Copyright 2009, American Chemical Society; (f) synthetic route of the atomically dispersed Mn-N-C catalysts by impregnation adsorption method.<sup>27</sup> Copyright 2018, Springer Nature.

In the solvothermal method, azides are used as intermediates, which can be used to synthesize more complex metal nitrides such as transition metal-doped nitride semiconductors. However, it is worth noting that azides are thermally unstable and extremely sensitive to shocks, which means that the appropriate protective measures should be taken during the synthesis process. The advantage of the solvothermal method is that the shape, crystallinity and size of the product can be controlled by solvent type and temperature, but the reaction takes a long time, which may lead to the agglomeration of nanoparticles. Therefore, attention should be paid to the control of conditions and time during the synthesis.<sup>21</sup>

### 3.3 Impregnation adsorption method

For the preparation of metal nitrides, impregnation adsorption is a very common method. The impregnation adsorption method first requires the synthesis of porous carbon carriers with optimal nitrogen doping, and then the target metal is adsorbed into the porous carbon carrier by impregnation adsorption, and finally  $\text{MN}_x$  catalyst can be obtained by thermal activation. ZIFs (porous crystalline materials) are a common precursor with a large specific surface area and many microporous structures. They are ideal adsorption materials, so ZIFs are often carbonized to obtain porous carbon carriers.<sup>26</sup> Li *et al.* prepared Mn-doped ZIF-8 precursor by combining Mn ions with Zn ions.<sup>27</sup> ZIF-8 with SOD topology constructed by  $\text{Zn}^{2+}$  and 2-methylimidazole can maintain high stability in high temperature solvents.<sup>133</sup> Mn-ZIF-8 derivatives were obtained by carbonization and pickling of manganese-doped precursors. The derived porous carbon can adsorb Mn sources and N sources. After thermal activation, a single-atom M-N-C catalyst (Fig. 3f) was prepared, which showed good ORR activity and stability in aqueous solution. In this process,

the content of Mn will affect the morphology and structure of carbon particles. Within a certain range (Mn content is less than 30 at%), the increase of Mn content will enhance the degree of graphitization in the carbon structure and increase the carbon particle size, but excessive Mn ions will interfere with the growth of ZIF nanocrystals. Ding *et al.* used  $\text{H}_2\text{PtCl}_6 \cdot 6\text{H}_2\text{O}$  and  $\text{FeCl}_3 \cdot 6\text{H}_2\text{O}$  as precursors and Vulcan XC-72 as a carbon carrier for the synthesis of bimetallic  $\text{PtFe}_3\text{N}$ .<sup>28</sup> After the immersion of Vulcan XC-72 in the solution of  $\text{H}_2\text{PtCl}_6 \cdot 6\text{H}_2\text{O}$  and  $\text{FeCl}_3 \cdot 6\text{H}_2\text{O}$  in a vacuum oven for several hours to prepare Pt-Fe/Vulcan XC-72, the  $\text{PtFe}_3\text{N}/\text{C}$  was successfully prepared by annealing Pt-Fe/Vulcan XC-72 in a tube furnace under a  $\text{H}_2/\text{Ar}$  atmosphere (350 °C) and  $\text{NH}_3$  (650 °C), respectively, for 2 hours. The prepared  $\text{PtFe}_3\text{N}/\text{C}$  showed high ORR catalytic activity (Fig. 4a). Because of the presence of strong covalent bonds, the ORR catalytic stability of  $\text{PtFe}_3\text{N}/\text{C}$  is greatly improved compared with Pt/C catalyst (Fig. 4b-d).<sup>28</sup>

The impregnation adsorption method can freely select the appropriate carrier to provide the required physical properties for the catalyst, and the synthesis steps of catalyst can be obviously subtracted. However, it is worth noting that the impregnation adsorption method often requires secondary heating, which makes the reaction more complicated and cannot be applied to large-scale or industrial production. Simplifying the synthesis process can greatly promote the application of impregnation adsorption method. As a more commonly used precursor in the impregnation adsorption method, the synthesis of ZIFs is more difficult and not suitable for large-scale production. As we all know, ZIFs are prone to agglomeration during the impregnation process, and this means the metal concentration in the catalyst cannot be high, which is not conducive to catalytic activity improvement of catalysts.<sup>26</sup>

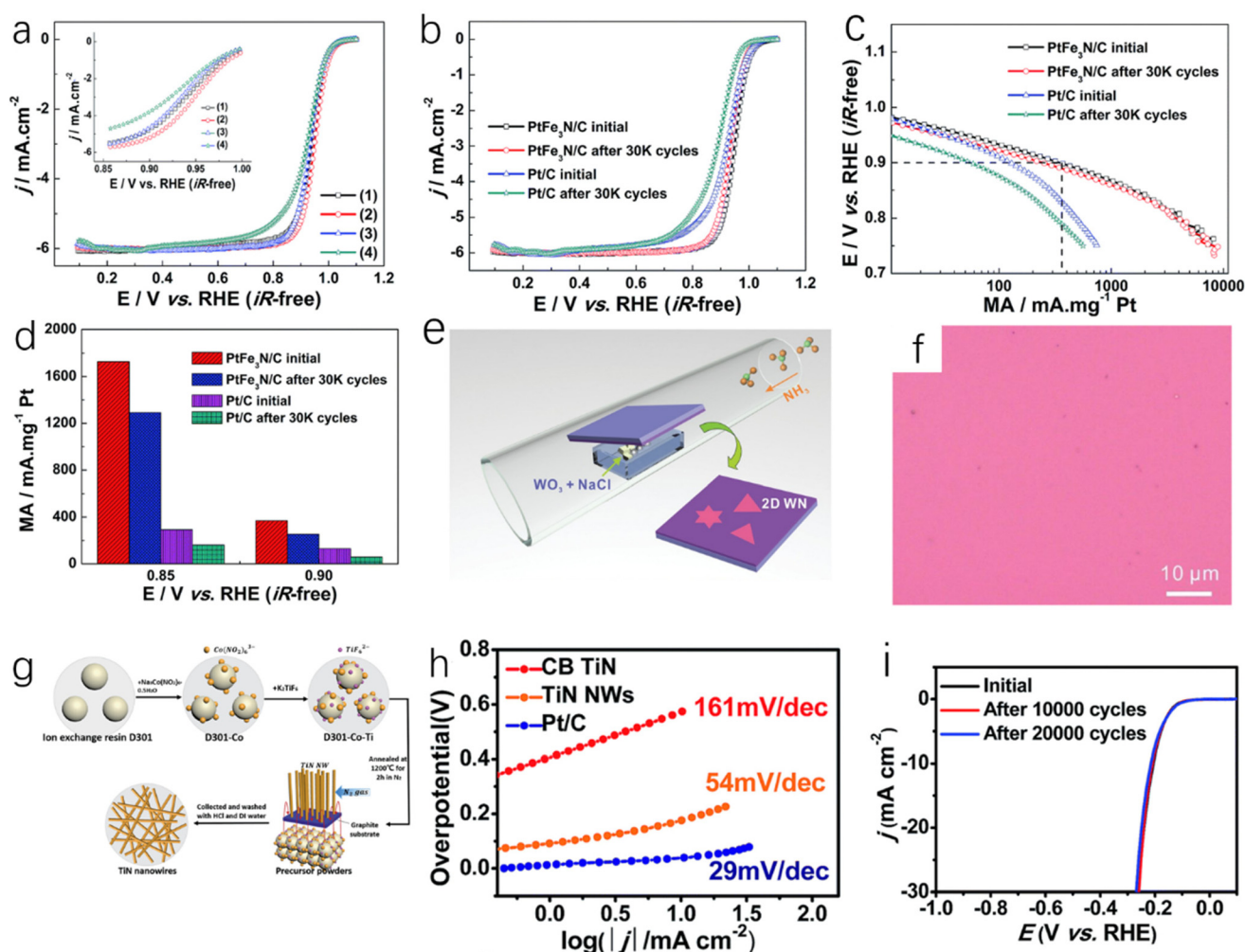


**Fig. 4** (a) ORR polarization curve of the catalyst in  $O_2$ -saturated  $0.1 \text{ mol L}^{-1} \text{ HClO}_4$  aqueous solution ( $25^\circ\text{C}$ , scanning rate  $5 \text{ mV s}^{-1}$ , rotation speed  $1600 \text{ rpm}$ ), (inset: high-magnification polarization curve); (b) ORR polarization curves of  $\text{PtFe}_3\text{N/C}$  and  $\text{Pt/C}$  catalysts before and after ADT in  $O_2$ -saturated  $0.1 \text{ mol L}^{-1} \text{ HClO}_4$  aqueous solution ( $25^\circ\text{C}$ , scan rate of  $5 \text{ mV s}^{-1}$ , rotation speed of  $1600 \text{ rpm}$ ); (c) comparison of mass activity (MA) before and after cycling; (d) comparison of mass activity of  $\text{PtFe}_3\text{N/C}$  and  $\text{Pt/C}$  before and after cycling at  $0.90 \text{ V}$  and  $0.85 \text{ V}$ .<sup>28</sup> Copyright 2015, Royal Society of Chemistry; (e) a schematic CVD synthesis of ultrathin WN; (f) optical image of the product grown on  $\text{SiO}_2/\text{Si}$  substrate (without salt).<sup>31</sup> Copyright 2019, Wiley-VCH; (g) synthetic route of TiN NWs; (h) Tafel plots of TiN NWs, CB TiN and Pt/C electrodes; (i) the stability test of TiN NWs catalyst carried out by potential cycling, which shows the initial polarization curve and the polarization curve after 10 000 and 20 000 potential cycles.<sup>32</sup> Copyright 2016, Royal Society of Chemistry.

### 3.4 Chemical vapor deposition method

Chemical vapor deposition (CVD) is a technique for producing solid powder precursors in the vapor phase and depositing thin films on a substrate. Based on chemical reactions or plasma-promoted chemical reactions, it has been widely used in the manufacturing methods of microelectronics and protective coatings of cermets.<sup>29</sup> Fix *et al.* reported that crystalline TiN and  $\text{Zr}_3\text{N}_4$  films were prepared by CVD technology with metal and diethylamino complexes under atmospheric pressure.<sup>30</sup> Wang *et al.* used  $\text{WO}_3$  and NaCl mixed powders as precursors and reacted with ammonia at a certain temperature to obtain WN crystals deposited on the substrate (Fig. 4e).<sup>31</sup> As shown in Fig. 4f, when no salt is used on the substrate, the growth and nucleation of WN cannot be observed, so salt

assistance plays an important role in the WN deposition process. Han *et al.* used the anion exchange resin D301 of  $\text{Co}(\text{NO}_2)_6^{3-}$  ion and  $\text{TiF}_6^{2-}$  ion (D301-Co-Ti) as a precursor,<sup>32</sup> as well as a titanium source and catalyst as shown in Fig. 4g. Then, a graphite rod substrate was placed on the top of the precursor powder. Finally, single-crystal nitrogen titanate nanowires (TiN NWs) were prepared after annealing at  $1200^\circ\text{C}$  for 2 h under a nitrogen atmosphere. The prepared TiN NWs are single-crystal structures and have uniform one-dimensional morphology, which gives them higher conductivity and a fast electron transport network. According to Tafel diagrams of TiN NWs, bulk TiN (CB TiN) and Pt/C (Fig. 4h), it can be found that although the HER catalytic activity of TiN NWs is lower than that of Pt/C, their HER catalytic activity is greatly improved compared with bulk TiN, and TiN NWs have high catalytic stability. After 10 000



cycles, the current density has no obvious change, and it only decreases slightly after 20 000 cycles (Fig. 4i).

Highly oriented, anisotropic or porous metal nitrides can be successfully prepared by the CVD method. In addition, some new metal nitrides can be fabricated by changing deposition conditions.<sup>33</sup> However, there are also some problems in the use of the CVD method; for example, it cannot deposit on a surface or a specific area, and its relatively low production rate leads to a long preparation cycle, which is not conducive to its industrial application.

### 3.5 Metal-organic framework material carbonization

The metal-organic framework (MOF) is a metal organic skeleton formed by connecting inorganic and organic building units. It has become an important precursor for the preparation of metal-based nanomaterials in the field of electrocatalysis.<sup>34</sup> MOF is a highly ordered multidimensional porous network material formed by bonding, or other forms, of metal ions or metal clusters with organic ligands.<sup>35</sup> Hu *et al.* studied the thermal decomposition of oxygen-free/nitrogen-containing manganese triazolate (MOF MET-2) as a precursor to prepare

manganese nitride.<sup>36</sup> The precursor was pyrolyzed/annealed at 525 °C and under a pure nitrogen atmosphere for 4 hours to obtain manganese nitride (Fig. 5a and b show the changes and reaction pathways, respectively, from the precursor to manganese nitride structure during this process). Wang *et al.* carbonized the manganese-containing molecular sieve-imidazole frameworks and accordingly obtained Co@Co<sub>4</sub>N/MnO-NC.<sup>37</sup> In addition, Wang *et al.* found that Fe-ZIF-8-CNTs were easily decomposed into Fe-N/C-CNT under a N<sub>2</sub> atmosphere. As shown in Fig. 5c, Fe-N/C-CNTs were successfully fabricated by placing Fe-ZIF-8-CNTs under a nitrogen atmosphere at 1000 °C,<sup>38</sup> and the introduction of carbon nanotubes could avoid the agglomeration of ZIFs (porous crystal materials) and improve the catalytic activity. Zhu *et al.* found that NENU-5 MOF can be used to synthesize molybdenum nitride nanoparticles under an ammonia atmosphere.<sup>39</sup> MOF-derived catalysts often have a better arrangement and adjustable porous structure than the original MOFs, which can provide more active sites for catalytic reactions.<sup>40–42</sup>

The key to the MOF carbonization method for TMN preparation is to synthesize the target MOF, but the MOF usually

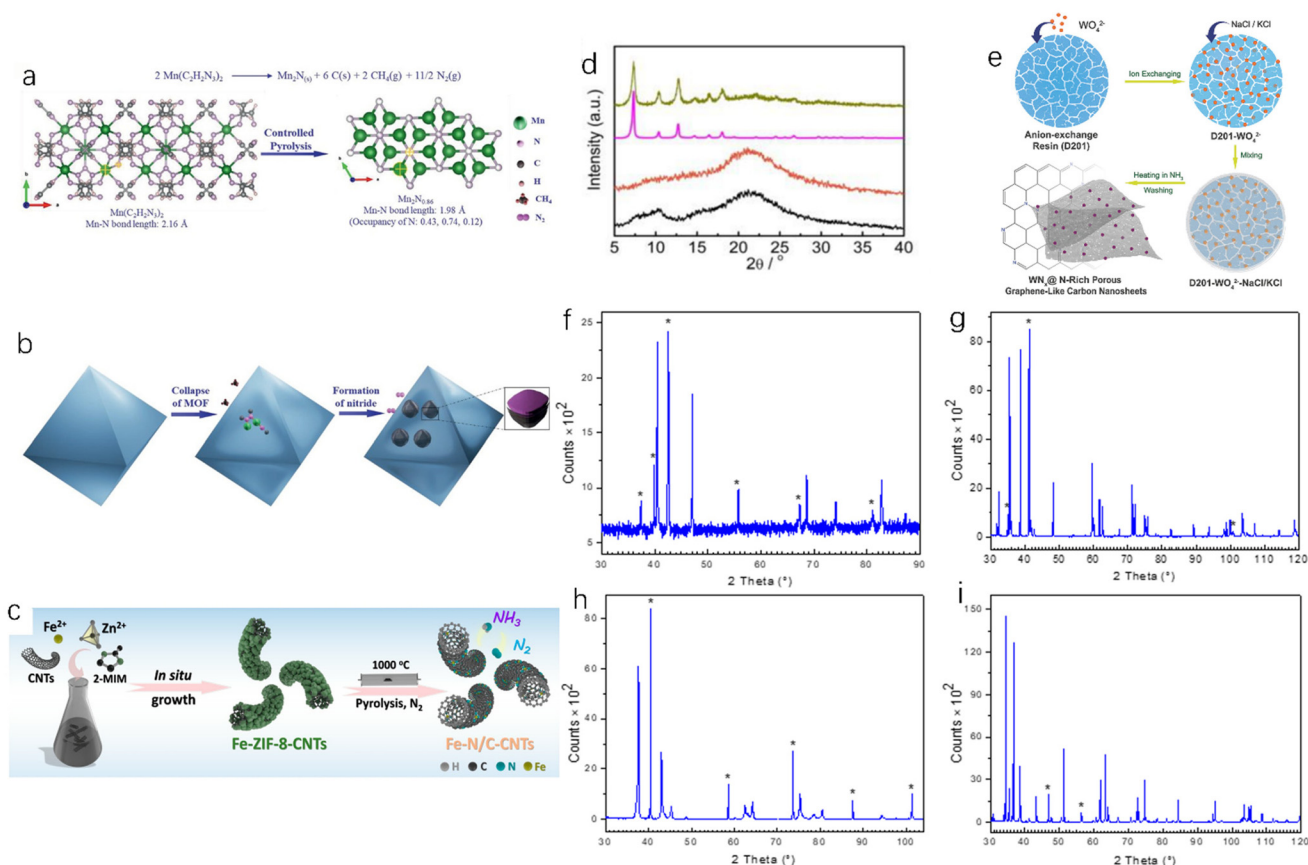


**Fig. 5** (a) The reaction of manganese triazolate to manganese nitride nanoparticles and the crystal structure of  $\text{Mn}(\text{C}_2\text{H}_2\text{N}_3)_2$  (0.5 cells) and  $\text{Mn}_2\text{N}_{0.86}$ ; (b) morphology evolution during pyrolysis.<sup>36</sup> Copyright 2021, Wiley-VCH; (c) synthesis of Fe-N/C-CNTs.<sup>38</sup> Copyright 2019, American Chemical Society; (d) XRD patterns of ZnCo-PPF-3 before and after reaction.<sup>43</sup> Copyright 2020, Springer Nature; (e) synthetic route of  $\text{WN}_x$ -NRPGC.<sup>45</sup> Copyright 2018, Wiley-VCH; (f) XRD pattern of  $\text{Mn}_4\text{N}$  ( $\text{Mn}_2\text{N}_{0.86}$  phase is represented by an asterisk); (g) XRD pattern of NbN (the asterisk represents  $\text{Nb}_8\text{N}_{6.8}$  phase); (h) XRD pattern of  $\text{Mo}_2\text{N}$  (the asterisk represents Mo phase); (i) XRD pattern of TaN (the asterisk represents  $\text{Ta}_2\text{N}_{0.86}$  phase).<sup>47</sup> Copyright 2022, International Information and Engineering Technology Association.

lacks the diversity of nanomorphology and the complexity of nanostructures, and most of the MOF materials are solid porous materials, which is not conducive to wide application. Future research directions could modify MOF materials on nano-micron structures to obtain more nanostructured MOFs. In addition, the stability of the MOF precursor will affect the synthesis of the catalyst. If the MOF precursor is too stable, the target product cannot be synthesized (Fig. 5d).<sup>43</sup> When the MOF linker contains oxygen and the metal reduction potential is less than a critical value, the product will not be a metal nitride but a metal oxide.<sup>44</sup> In addition, the intermediates of MOF pyrolysis are easily disturbed by H<sub>2</sub>O and O<sub>2</sub> to form oxides or hydroxides, so it is necessary to ensure that the environment is free of H<sub>2</sub>O and O<sub>2</sub>. High porosity is the advantage of MOF, but the porous structure often means that the density is reduced, the mechanical strength is reduced, and it is easy to damage, which is not conducive to use in wider practical applications.<sup>15</sup>

### 3.6 Other synthetic methods

In addition to the commonly used methods mentioned above, there are some other methods that can be used to synthesize TMNs. Reducing the synthesis steps or achieving multiple functions in one step is conducive to simplifying the production process. Zhu *et al.* used a technology based on resin ion exchange to prepare strong coupling composites,<sup>45</sup> and synthesized nitrogen-rich porous graphene-like carbon nanosheets (WN<sub>x</sub>-NRPGC) under a NH<sub>3</sub> atmosphere. In the calcination process, the transformation of resin skeleton to the carbon nanostructure, the formation of doped N atoms, WN<sub>x</sub> nanostructures, and the uniform anchoring of the surface of carbon nanosheets were realized as shown in Fig. 5e. Kerdoud *et al.* used some simple methods to synthesize Mn<sub>4</sub>N, NbN, MoN, TaN and so on.<sup>47</sup> Mn<sub>4</sub>N was obtained by heating magnesium powder in NH<sub>3</sub> at 600 °C for 3 hours. NbN was prepared by gas phase reaction of NbCl<sub>5</sub> and NH<sub>3</sub> at 200–1300 °C. MoN was obtained after the passivation treatment of the sample that was prepared by MoO<sub>3</sub> reacting with nitrogen/hydrogen mixed gas at a predetermined temperature. TaN is obtained by reacting TaCl<sub>5</sub> with sodium to obtain a powder, which is then heated in nitrogen at 900 °C for 24 hours. In order to determine the specific compositions of the above products, XRD analysis was performed as shown in Fig. 5f–i. The second phase was usually produced during the synthesis process, namely nitrogen-deficient compounds (Mn<sub>2</sub>N<sub>0.86</sub>, Nb<sub>8</sub>N<sub>6.8</sub> and Ta<sub>2</sub>N<sub>0.86</sub>, Mo-MoN). This may be due to the fact that metal nitrides are mostly interstitial compounds, which make nitrides diverse. It is very important to reduce the equipment requirements in actual production, such as reducing the synthesis temperature, pressure, and other environmental conditions. Wang *et al.* mixed high-purity sodium molybdate and hexagonal manganese nitride at a molar ratio of 1:2 and pressed them into cylindrical spherical clusters,<sup>46</sup> and then used a DS6 × 14 MN cubic press to rapidly heat them up to 1300 °C at 3.5–5 GPa for 20 minutes until they were directly quenched to room temperature. Finally, δ-MoN was success-

fully obtained. This method can produce δ-MoN only at moderate pressure (3.5 GPa), so it can be applied even in large-scale or industrial production. The hydrothermal method is similar to solvothermal method. The solvent used in the hydrothermal method is water, so the cost is low. Grains with complete development, small particle size, uniform distribution and light particle agglomeration can be prepared. Xie *et al.* prepared BFNTO<sub>–x</sub>(Bi<sub>7</sub>Fe<sub>3–x</sub>Ni<sub>x</sub>Ti<sub>3</sub>O<sub>21</sub>) powder by the hydrothermal method at 200 °C,<sup>48</sup> and the obtained product nanosheets were vertically arranged. In addition to ammonia and nitrogen as a nitrogen source, some nitrogen-containing compounds can also be used as one of the nitrogen sources. Zhao *et al.* used melamine as a nitrogen source to react with metal oxides to prepare metal nitrides.<sup>49</sup> They mixed chromium oxide and excess melamine and pressed it into granules, then reduced the pressure in the ampoule to 3 × 10<sup>–6</sup> Pa sealed preservation, and finally heated it at 650 °C for 1 hour. CrN was obtained after cooling the sample to room temperature. Various metal nitrides such as VN and TiN were also obtained by this method. It is worth noting that the wide availability and high yield of melamine and metal oxides mean that this method can be applied in large-scale production.

In summary, for the synthesis of single-metal nitrides, annealing or heat treatment is generally performed in a nitrogen source. The nitrogen source can be nitrogen, ammonia, *etc.* For example, single-metal nitrides can be obtained by heat treatment of metal oxides or precursors under an ammonia atmosphere, which is also a widely used method. CVD and solvothermal method also can be used to synthesize single-metal nitrides by solution process. CVD can deposit metals inside nanostructures. The advantage of the solvothermal method is that the size and shape of products are easy to control. However, a major disadvantage of the solution process is that the reaction speed is slow and it needs a long synthesis time.<sup>21,33,50</sup> Bimetallic nitrides are generally prepared by the ammoniation of ternary metal precursors. Nitride materials with small particle size, uniform distribution, uniform composition and high activity can be prepared by using appropriate precursors.<sup>50</sup> There are many methods for the synthesis of composite metal nitrides, such as the impregnation adsorption method and MOF carbonization method. The impregnation adsorption method usually uses ZIFs (porous crystal materials) as the carrier. The advantage of this synthesis method is that the appropriate carrier can provide good physical properties for the catalyst, but the secondary heating makes the reaction complicated. The rule of the above method is to use MOF as a precursor to obtain the product after treatment. The advantage of MOF is high porosity, and the porous structure will lead to a decrease in the density of product.<sup>15,26,50</sup>

Although many synthetic methods have been applied to the synthesis of metal nitrides, these methods have certain defects. Finding a better synthesis method requires the following aspects. Firstly, simplify the synthesis step or implement multiple functions in one step. Overly complex synthesis steps are often difficult to control and difficult to apply in industrial



production. Secondly, the widely used nitrogen sources are ammonia and nitrogen. However, ammonia is toxic and unstable, and the inertness of nitrogen is not easy to overcome. Therefore, it is necessary to find other nitrogen sources, such as urea. Thirdly, a major disadvantage of metal nitride synthesis is that the synthesis conditions are mostly high temperature and high pressure, which need high equipment requirements. It is a huge challenge to synthesize metal nitrides with high activity under mild conditions. Finally, the particle size and shape of the product should be well controlled. It is difficult to control the morphology of the product with most of the current synthesis methods, due to by-products, heat treatment problems or the influence of water and oxygen in the air. It is very important to overcome these problems. In addition, for different metal nitrides, the most suitable synthesis method can achieve the best activity.

## 4. Applications of metal nitrides in the field of electrocatalysis

### 4.1 Hydrogen evolution reaction

The hydrogen evolution reaction (HER) is the cathode reaction of water splitting to produce hydrogen. A good HER catalyst can greatly reduce the overpotential. Noble metals such as Pt are often used as catalysts in HER, but their high price limits their application. Metal nitrides are one of the alternatives to precious metal catalysts and have excellent HER activity. Table 1 lists the HER activities of some metal nitrides and precious metal catalysts in different electrolytes. In the design and development of HER catalysts, the process of hydrogen production and hydrogen adsorption should be considered. In addition, it is widely believed that hydrogen adsorption free energy ( $\Delta G_{H^*}$ ) is one of evaluation criteria for HER performance. Lower  $\Delta G_{H^*}$  is beneficial for obtaining better HER activity. For example,  $\Delta G_{H^*}$  of noble metal catalysts such as Pt is close to 0, which can be used as a guide for the development of efficient HER catalysts.<sup>7,50,54</sup>

**Table 1** The HER catalytic performance comparisons of various TMNs and Pt/C catalysts

Catalyst	Electrolyte	$\eta_{10}$ (mV)	Tafel slope (mV dec <sup>-1</sup> )	Ref.
Co <sub>3</sub> Mn <sub>3</sub> N	0.5 M H <sub>2</sub> SO <sub>4</sub>	108	80	62
Co <sub>3</sub> Mn <sub>3</sub> N <sub>0.5</sub>	0.5 M H <sub>2</sub> SO <sub>4</sub>	117	76	62
Ni <sub>3</sub> N <sub>1-x</sub> /NF	1.0 M KOH	55	54	115
RuCo@NC	1.0 M KOH	28	31	116
Mo <sub>5</sub> N <sub>6</sub>	1.0 M KOH	94	66	117
Ni <sub>3</sub> N@CQDs	1.0 M KOH	69	108	118
Ni <sub>3</sub> N	1.0 M KOH	59	59.79	137
Ni <sub>3</sub> N@VNNF	1.0 M KOH	56	47	70
NiMoN <sub>x</sub> /C	0.1 M HClO <sub>4</sub>	—	35.9	6
Co <sub>2</sub> N <sub>0.67</sub> /MoO <sub>2</sub> /MF-500	1.0 M KOH	75.2	150.3	72
Cu <sub>3</sub> N	1.0 M NaOH	149.18	63.28	55
Pt/C	1.0 M KOH	30.5	31.0	72
Pt/C/NF	1.0 M KOH	46	45	115

Single-metal nitride is the simplest metal nitride and the earliest studied metal nitride. For example, Fig. 6a shows the activity of TiN and Pt-modified glassy carbon electrode in 0.5 M H<sub>2</sub>SO<sub>4</sub>. Although the hydrogen evolution activity of TiN is slightly weaker than that of Pt, it still has high hydrogen evolution activity and excellent corrosion resistance.<sup>51</sup> Han *et al.* synthesized single-crystal titanium nitride nanowires (TiN NWs) by chemical vapor deposition.<sup>32</sup> In 1.0 M HClO<sub>4</sub> solution, the electrochemical activities of TiN nanowires deposited on glassy carbon (GC) electrode, TiN deposited on commercial bulk carbon electrode (CB TiN), bare glassy carbon electrode and Pt/C were tested. As shown in Fig. 6b, when the current density is 1 mA cm<sup>-2</sup>, the initial overpotential of TiN nanowires is about 92 mV, while CB TiN shows a low HER activity. The onset overpotential of CB TiN is about 405 mV, which is 313 mV higher than that of TiN nanowires. This may be due to low specific area of CB TiN, so the specific surface area is an important factor affecting the catalytic activity. Fig. 6c shows that the Tafel slope of TiN NWS is 54 mV dec<sup>-1</sup> and the Tafel slope of CB TiN is 161 mV dec<sup>-1</sup>. It can be seen that although the activity of TiN NWs is lower than that of Pt, it has been greatly improved compared with CB TiN. This can be explained using electrochemical impedance spectroscopy. As shown in Fig. 6d, the charge transfer resistance of TiN NWs is smaller than that of CB TiN, which indicates that TiN NWs have a higher charge transfer rate. As a metastable semiconductor, the excellent performance of copper nitride makes Cu<sub>3</sub>N an effective hydrogen evolution catalyst.<sup>52,53</sup> Aparna *et al.* studied the HER activity of Cu<sub>3</sub>N under alkaline conditions (1.0 NaOH).<sup>55</sup> As shown in Fig. 6h, Cu<sub>3</sub>N shows a very high catalytic activity for HER. Compared with Cu<sub>2</sub>O, the onset potential of Cu<sub>3</sub>N is 0.085 V, which is lower than that of Cu<sub>2</sub>O at a current density of 10 mA cm<sup>-2</sup>. For TMNs, oxygen doping is inevitable. Some studies have shown that oxygen doping can lead to catalyst deactivation and reduce catalytic performance.<sup>56</sup> However, some studies have also found that partial oxidation of metal nitrides can enhance their hydrogen evolution performance. Adimi *et al.* studied whether the presence of oxygen impurities would affect the hydrogen evolution catalytic performance of VN.<sup>57</sup> VN is a promising catalyst because the transfer charge between vanadium and nitrogen can cause the density of states (DOS) on the surface of VN to be similar to that of Pt. In the oxygen-doped structure, oxygen will affect the electronic structure of vanadium and nitrogen (Fig. 6e and f). As shown in Fig. 6g, increasing the oxidation rate of the VN surface slightly increases the total density of states near the Fermi level, which will benefit to obtain better hydrogen evolution catalytic performance, and these authors found that a single layer of VO could act as a surface oxide activation layer (SOAL) on the VN surface. However, it is worth noting that for some TMNs, the formation of a thin oxide layer on the surface will prevent further oxidation and has little effect on the conductivity, which means that the formation of an oxide layer can improve the stability of TMNs and has little effect on the catalytic activity.<sup>58</sup>

Bimetallic nitrides have better catalytic activity than monometallic nitrides; Jaksic *et al.* proposed that there was a hypo-

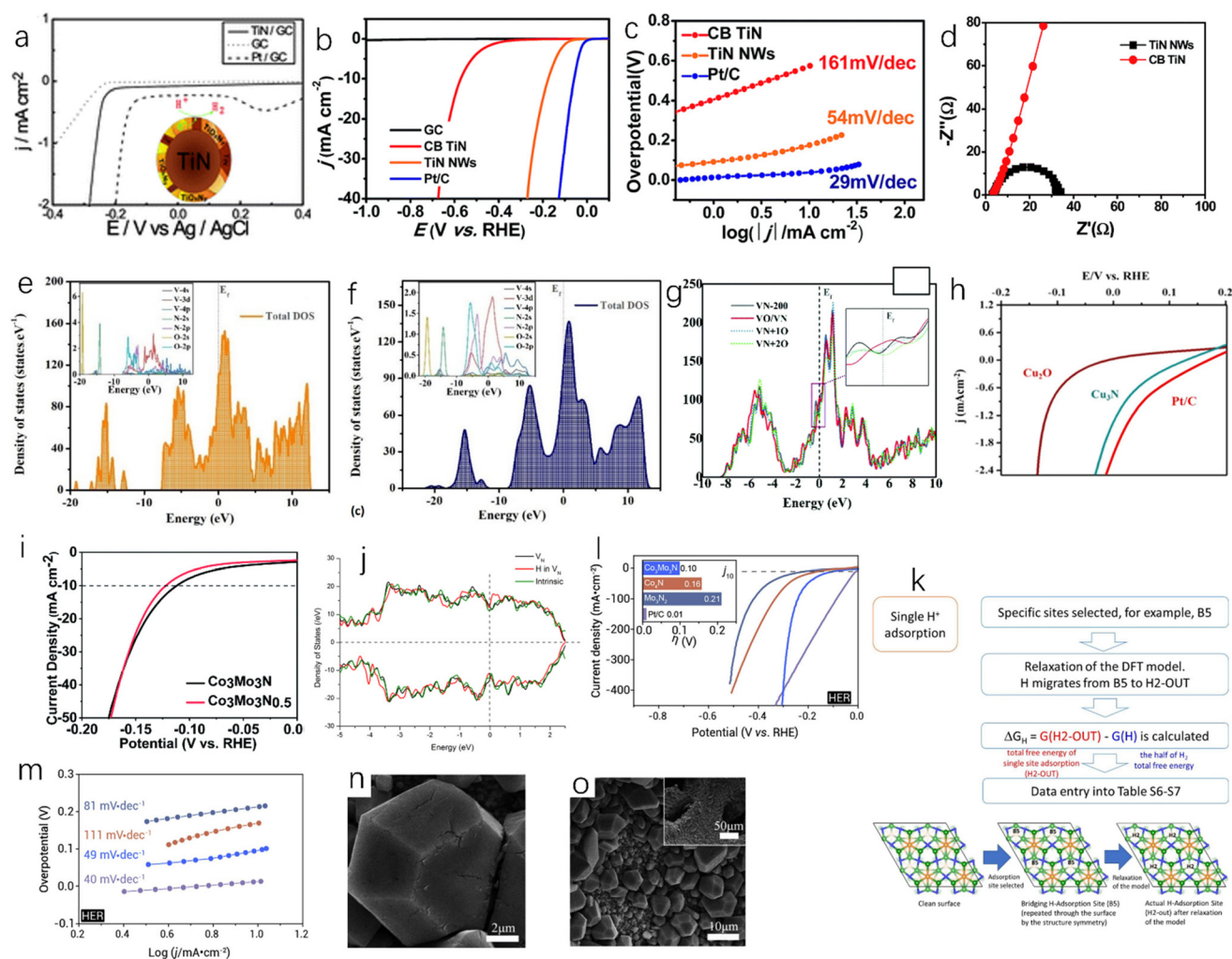


**Fig. 6** (a) HER linear sweep voltammograms of GC, TiN-modified GC and Pt-modified GC electrodes in 0.5 M H<sub>2</sub>SO<sub>4</sub> at a scan rate of 5 mV s<sup>-1</sup>.<sup>51</sup> Copyright 2012, Royal Society of Chemistry; (b) the polarization curves of TiN NWs electrode in 1 M HClO<sub>4</sub> and CB TiN, commercial Pt/C, bare glassy carbon (GC) electrode in 1 M HClO<sub>4</sub> (after IR correction); (c) Tafel plots corresponding to TiN NW, CB TiN and Pt/C electrodes; (d) Nyquist plots of TiN NWs electrode and CB TiN electrode measured at an overpotential of 0.3 V.<sup>32</sup> Copyright 2016, Royal Society of Chemistry; (e) the density of states of VN (112) surface with single-doped O and (f) double-doped O; (g) comparison of total DOS near the Fermi level of different catalysts.<sup>57</sup> Copyright 2021, Royal Society of Chemistry; (h) the steady-state polarization diagrams of Cu<sub>3</sub>N (160 ml min<sup>-1</sup> ammonia flow rate, synthesized at 300 °C), Cu<sub>2</sub>O and Pt/C.<sup>55</sup> Copyright 2022, Springer nature; (i) electrochemical studies of Co<sub>3</sub>Mo<sub>3</sub>N and Co<sub>3</sub>Mo<sub>3</sub>N<sub>0.5</sub> in 0.5 M H<sub>2</sub>SO<sub>4</sub> solution; (j) the total density of states (DOS) of the intrinsic surface (green line), the surface with a N-vacancy (black line), and the surface with a H filled in the N-vacancy (red line); (k) a schematic representation of the algorithm taken to calculate  $G_{\text{Hads}}$  for a single site adsorption model.<sup>62</sup> Copyright 2022, Royal Society of Chemistry; (l) comparison of the overpotentials required for the polarization curve (inset) of HER (10 mV s<sup>-1</sup>) to reach 10 mA cm<sup>-2</sup> in 1.0 M KOH solution; (m) the corresponding HER Tafel slope.<sup>63</sup> Copyright 2021, ScienceDirect; low (n) and high (o) resolution SEM images of N-NiCoP/NCF.<sup>64</sup> Copyright 2019, ScienceDirect.

hyper-d-electronic interactive effect between two metals, which will produce a synergistic effect between different metals, which will enhance the HER catalytic activity of the catalyst,<sup>128</sup> and the presence of two metals will provide more active sites and high electronic conductivity, which is conducive to the catalytic reactions.<sup>59–61</sup> Sun *et al.* used the linear sweep voltammetry (LSV) test to study the catalytic activities of Co<sub>3</sub>Mo<sub>3</sub>N and Co<sub>3</sub>Mo<sub>3</sub>N<sub>0.5</sub> at 10 mA cm<sup>-2</sup> in 0.5 M H<sub>2</sub>SO<sub>4</sub>,<sup>62</sup> and the results showed that the overpotentials of Co<sub>3</sub>Mo<sub>3</sub>N and Co<sub>3</sub>Mo<sub>3</sub>N<sub>0.5</sub> were 108 ± 8 mV and 117 ± 12 mV, respectively (Fig. 6i), and both Co<sub>3</sub>Mo<sub>3</sub>N and Co<sub>3</sub>Mo<sub>3</sub>N<sub>0.5</sub> catalysts had a

cathode current density of more than 500 mA cm<sup>-2</sup>, indicating high HER catalytic activity. As shown in Fig. 6j, the Mo site near the N site exhibits DOS (total density of states) independent of the N-site occupation, and the role of N as an active site is extremely limited, which makes Co<sub>3</sub>Mo<sub>3</sub>N and Co<sub>3</sub>Mo<sub>3</sub>N<sub>0.5</sub> have very similar electrocatalytic performance, and the role played by N as an active site is extremely limited. The DFT (density functional theory) simulation of Co<sub>3</sub>Mo<sub>3</sub>N was carried out. Fig. 6k is based on a single adsorption site model. In this simulation, the  $\Delta G_{\text{H}}$  of the hollow H<sub>2</sub>-OUT site is 0.03 eV, which indicates that the activity of Co<sub>3</sub>Mo<sub>3</sub>N is close to the

thermodynamic optimal value. Yuan *et al.* also studied  $\text{Co}_3\text{Mo}_3\text{N}$ .<sup>63</sup> Under alkaline conditions (1.0 M KOH), at a current density of  $10 \text{ mA cm}^{-2}$ , the overpotential of  $\text{Co}_3\text{Mo}_3\text{N}$  is  $-0.10 \text{ V}$ , that of Pt/C is  $-0.01 \text{ V}$ , that of  $\text{Co}_4\text{N}$  is  $-0.16 \text{ V}$ , and that of  $\text{Mo}_3\text{N}_4$  is  $-0.21 \text{ V}$  as shown in Fig. 6l. The current densities of  $\text{Co}_3\text{Mo}_3\text{N}$  and Pt/C will reach the same value at  $-0.30 \text{ V}$ , which means that  $\text{Co}_3\text{Mo}_3\text{N}$  has excellent catalytic performance at a large current density. The Tafel slope of  $\text{Co}_3\text{Mo}_3\text{N}$  ( $49 \text{ mV dec}^{-1}$ ) is lower than those of  $\text{Co}_4\text{N}$  ( $111 \text{ mV dec}^{-1}$ ) and  $\text{Mo}_3\text{N}_2$  ( $81 \text{ mV dec}^{-1}$ ) (Fig. 6m). The phosphorization of bimetallic nitride also has excellent HER performance. Zhang *et al.* prepared a polyhedral N-doped Ni-Co phosphide (N-NiCoP).<sup>64</sup> The HER catalytic activity test was performed under alkaline conditions (1.0 M KOH), and the overpotential of N-NiCoP/NCF was only  $78 \text{ mV}$  at a current density of  $10 \text{ mA cm}^{-2}$ . Observing the SEM image of N-NiCoP/NCF (Fig. 6n and o), cracks appeared on the surface of the catalyst, which would expose a large reaction area during the electrolysis process, which could improve the HER catalytic activity.

The composite material formed by coupling of transition metal nitrides and carbon materials has excellent HER catalytic performance, as the coupling between the components can increase the active site and enhance the charge transfer. Doping with nitrogen can improve the conductivity of the carbon material, and the carbon adjacent to the nitrogen dopant can be used as the active site to enhance the  $\text{H}^*$  adsorption, thereby enhancing the HER activity, and the incorporation of nitrogen atoms can overcome the instability of metal carbides.<sup>45,65,66</sup> Zhu *et al.* prepared tungsten nitride ( $\text{WN}_x$ ) nanocomposites supported on nitrogen-rich porous graphene-like carbon nanosheets ( $\text{WN}_x\text{-NRPGC}$ ),<sup>45</sup> which have excellent catalytic activity for HER in an acidic electrolyte. Graphene-based amorphous carbon nanosheets have hierarchical structures. This hierarchical structure has efficient electron diffusion capabilities, and  $\text{WN}_x$  nanostructures can provide a large number of active sites, which are beneficial for HER catalytic performance.<sup>67</sup> The  $\text{WN}_x\text{-NRPGC}$  composite has a high specific surface area of  $304 \text{ m}^2 \text{ g}^{-1}$  and a large pore volume of  $0.35 \text{ cm}^3 \text{ g}^{-1}$ , which facilitates the penetration of liquid electrolytes and provides a large number of active sites. Compared with WN, the  $\text{WN}_x\text{-NRPGC}$  showed higher HER catalytic activity. As shown in Fig. 7a, the initial overpotential and the overpotential at  $10 \text{ mA cm}^{-2}$  of WN were  $331 \text{ mV}$  and  $492 \text{ mV}$ , respectively, while  $\text{WN}_x\text{-NRPGC}$  could reduce the initial overpotential by  $123 \text{ mV}$  and the overpotential at  $10 \text{ mA cm}^{-2}$  by  $255 \text{ mV}$  under the same conditions. WN as catalyst showed poor HER catalytic activity, which may be due to its fewer active sites, poor conductivity and surface properties. The Tafel slope of  $\text{WN}_x\text{-NRPGC}$  ( $86 \text{ mV dec}^{-1}$ ) is lower than that of bulk WN ( $175 \text{ mV dec}^{-1}$ ) (Fig. 7b), which also indicates that the HER catalytic activity of  $\text{WN}_x\text{-NRPGC}$  is greatly improved compared with bulk WN. In addition,  $\text{WN}_x\text{-NRPGC}$  has a higher electrochemical active surface area (ECSA) than bulk WN. As shown in Fig. 7c–e, using electrochemical double layer capacitance ( $C_{\text{dl}}$ ) to estimate ECSA, the  $C_{\text{dl}}$  of  $\text{WN}_x\text{-NRPGC}$  ( $16.6 \text{ mF cm}^{-2}$ ) is higher than that of bulk WN, and

the high  $C_{\text{dl}}$  indicates that the  $\text{WN}_x\text{-NRPGC}$  has a higher ECSA. Graphitic carbon nitride ( $\text{g-C}_3\text{N}_4$ ) has excellent electrochemical properties. Wang *et al.* synthesized coral-like  $\text{Ni/N}_3\text{C}_4\text{-0.10}$ ,<sup>68</sup> as shown in Fig. 7g and h. The  $\text{Ni/N}_3\text{C}_4\text{-0.10}$  catalyst has a coral-like structure (Fig. 7f shows a scanning electron microscope image of pure Ni), which is beneficial for the improvement of HER activity. The Tafel slope of  $\text{Ni/C}_3\text{N}_4\text{-0.10}$  is  $128 \text{ mV dec}^{-1}$ , which is lower than those of  $\text{Ni/C}_3\text{N}_4\text{-0.05}$  ( $143 \text{ mV dec}^{-1}$ ),  $\text{Ni/C}_3\text{N}_4\text{-0.15}$  ( $136 \text{ mV dec}^{-1}$ ) and  $\text{Ni/C}_3\text{N}_4\text{-0.20}$  ( $160 \text{ mV dec}^{-1}$ ), indicating that the catalytic kinetic performance of  $\text{Ni/C}_3\text{N}_4\text{-0.10}$  with coral-like structure is better than that of other  $\text{Ni/N}_3\text{C}_4$  composite catalysts.

In addition to the nitrogen-carbon composite material, some other types of TMN catalysts also have good application prospects. Murthy *et al.* found that Cu-doped molybdenum nitride films have superior HER catalytic activity (Fig. 7i) and stability (Fig. 7j) in near-neutral ( $\text{pH} = 5$ ) solution,<sup>69</sup> and the HER selectivity can reach 95% (Fig. 7k). Zhou *et al.* obtained a new and efficient  $\text{Ni}_3\text{N@VN-NF}$  composite catalyst by nitriding  $\text{NiV-LDH}$  precursor.<sup>70</sup> Compared with  $\text{Ni}_3\text{N-NF}$  and  $\text{VN-NF}$ , the  $\text{Ni}_3\text{N@VN-NF}$  exhibits excellent HER catalytic performance in 1.0 M KOH. As shown in Fig. 7l and m, the overpotential of  $\text{Ni}_3\text{N@VN-NF}$  at  $10 \text{ mA cm}^{-2}$  is  $56 \text{ mV}$  and the Tafel value is only  $47 \text{ mV dec}^{-1}$ . Zhuang *et al.* encapsulated the dispersed  $\text{Co}_2\text{P}$  in N, P-doped graphene to obtain  $\text{Co}_2\text{P@NPG}$  nanomaterials.<sup>71</sup> It has excellent HER catalytic activity and stability. As shown in Fig. 7n and o, the  $\text{Co}_2\text{P@NPG}$  shows a low overpotential of  $45 \text{ mV}$  at a current density of  $1 \text{ mA cm}^{-2}$  and a small Tafel slope of  $58 \text{ mV dec}^{-1}$ . The HER catalytic activity of  $\text{Co}_2\text{P@NPG}$  only slightly decreases after 10 000 cycles. As we all know, cheap, clean, and efficient catalysts are of great importance in practical applications. Tong *et al.* used  $\text{H}_2\text{O}_2$  to treat Mo-loaded cobalt hydroxide carbonate nanowires as precursors,<sup>72</sup> and successfully obtained  $\text{Co}_2\text{N}_{0.67}/\text{MoO}_2/\text{MF}$  by the nitridation of the above precursors under an ammonia atmosphere. The  $\text{Co}_2\text{N}_{0.67}/\text{MoO}_2/\text{MF}$  exhibits higher HER catalytic activity than  $\text{Co}_2\text{N}_{0.67}/\text{MF}$  at a current density of  $10 \text{ mA cm}^{-2}$ . The overpotential of  $\text{Co}_2\text{N}_{0.67}/\text{MoO}_2/\text{MF}$  is only  $75.2 \text{ mV}$  at  $10 \text{ mA cm}^{-2}$ , which is much lower than that of  $\text{Co}_2\text{N}_{0.67}/\text{MF}$  ( $150.6 \text{ mV}$ ). The introduction of  $\text{MoO}_2$  film can accelerate the transfer of interfacial charge and increase the specific surface area, providing more HER active sites for the catalytic reaction.

In summary, transition metal nitrides exhibit good application prospects and high HER catalytic activity and stability in acidic or alkaline electrolytes, and are excellent substitutes for noble metal catalysts. The shrinkage of the d-band gives TMNs similar properties to the precious metal catalysts, which makes TMNs have better thermal stability, chemical stability and electronic conductivity. However, it is worth noting that although transition metal nitrides have made great progress, their catalytic activity and stability are still not suitable for commercial applications compared with precious metal catalysts. The experimental conditions are mostly at a small current density. When TMNs with excellent catalytic activity and stability under experimental conditions are applied to high-current industrial production, they usually do not have



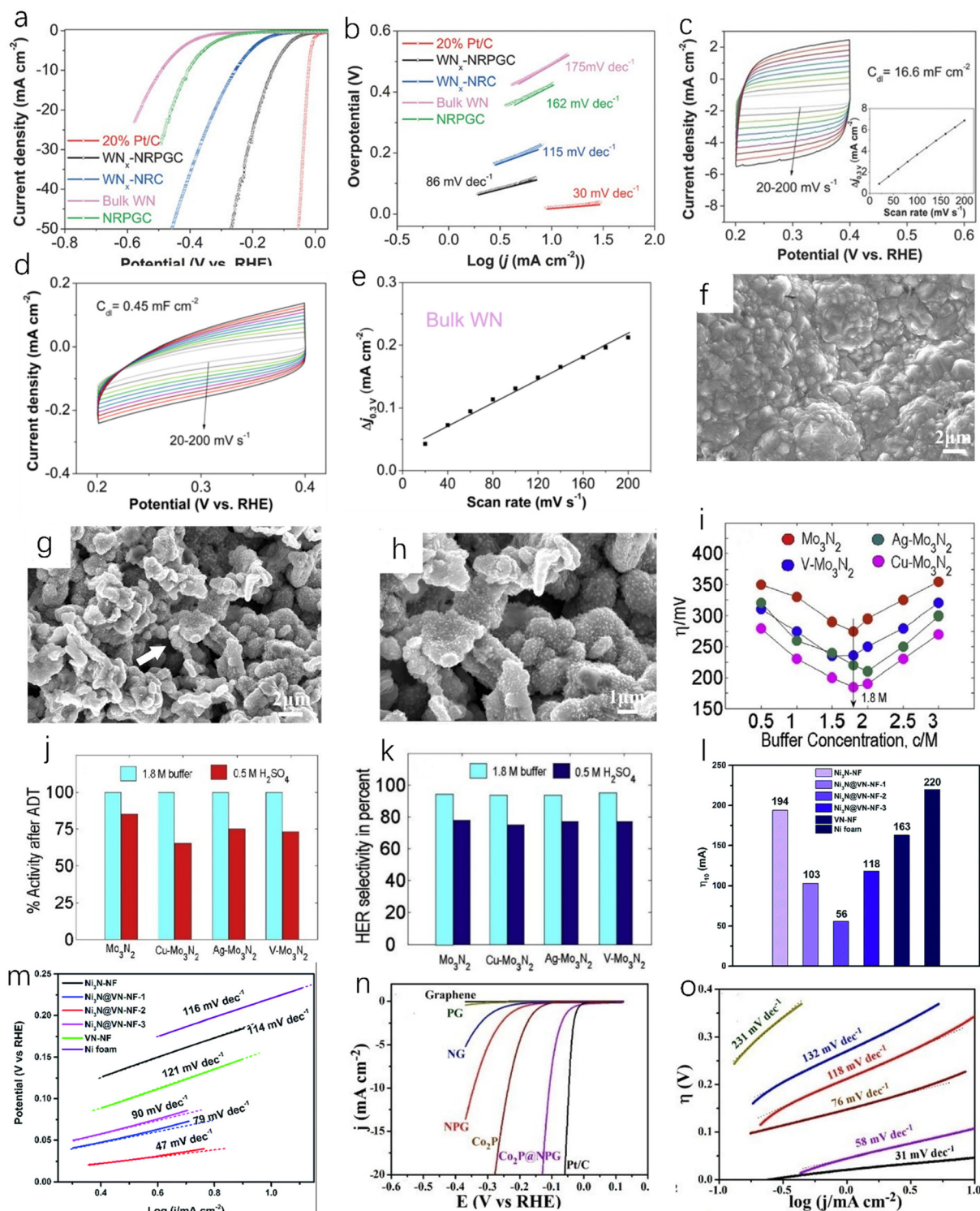


**Fig. 7** (a) The polarization curve of *iR* in 0.5 M H<sub>2</sub>SO<sub>4</sub> after compensation at a scan rate of 5 mV s<sup>-1</sup>; (b) Tafel plots of WN<sub>x</sub>-NRPGC, WN<sub>x</sub>-NRC, NRPGC, bulk WN and 20% Pt/C catalysts. (c) CVs of WN<sub>x</sub>-NRPGC at different rates from 20 to 200 mV s<sup>-1</sup> in the potential range of 0.2–0.4 V. Inset: linear fitting of the capacitive currents versus CV scan rates for WN<sub>x</sub>-NRPGC; (d and e) CVs and the corresponding linear fitting of the capacitive currents vs. CV scan rates for bulk WN NRPGC.<sup>45</sup> Copyright 2018, Wiley-VCH; (f) SEM image of pure Ni catalyst; (g) SEM image of Ni/C<sub>3</sub>N<sub>4</sub>-0.10 catalyst; (h) high-resolution SEM image of Ni/C<sub>3</sub>N<sub>4</sub>-0.10 catalyst.<sup>68</sup> Copyright 2017, American Chemical Society; (i) effect of buffer concentration on the overpotentials of various catalysts for HER; (j) the bar graph shows the activity loss of nitride films after ADT in 1.8 M buffer and 0.5 M H<sub>2</sub>SO<sub>4</sub>; (k) HER selectivity of different Mo<sub>3</sub>N<sub>2</sub> films in 1.8 M buffer and 0.5 M H<sub>2</sub>SO<sub>4</sub>.<sup>69</sup> Copyright 2018, ScienceDirect; the overpotentials (l) and (m) Tafel slopes of Ni<sub>3</sub>N-NF, VN-NF, pure nickel foam and Ni<sub>3</sub>N@VN-NF composites with different Ni/V molar ratios at 10 mA cm<sup>-2</sup>.<sup>70</sup> Copyright 2019, Royal Society of Chemistry; (n) the polarization curves of glassy carbon electrode modified with G-900, NG-900, PG-900, NPG-900, Co<sub>2</sub>P clusters, Co<sub>2</sub>P@NPG-900 and 20 wt% Pt/C, respectively, in 0.5 M H<sub>2</sub>SO<sub>4</sub> solution; (o) the Tafel slopes of various catalysts.<sup>71</sup> Copyright 2016, American Chemical Society.

long-term stability and activity. In HER, TMNs often lead to a decrease in HER catalytic activity due to surface oxidation; especially in practical applications the environment is mostly harsh (compared with experimental conditions), and many measurements of TMN activity do not consider this.<sup>14</sup> In future research, it is necessary to pay attention to the activity measurement of catalysts at high current densities and in harsh environments.

## 4.2 Application in oxygen evolution reaction

The oxygen evolution reaction (OER) is an anodic reaction of water splitting to produce hydrogen. It is a four-electron-proton coupling reaction, which is more complex than HER and requires higher energy (greater overpotential) to overcome kinetic obstacles. Therefore, OER is often regarded as the kinetic bottleneck of the water-splitting reaction.<sup>73,74</sup> Unlike in an acidic system, OER is easier to perform in alkaline electrolytes because water ionization occurs before the catalytic reaction in alkaline electrolytes. Some noble metal oxides such as RuO<sub>2</sub> and IrO<sub>2</sub> have excellent OER catalytic performance, but the high price limits their wide application. Transition metal nitrides are a good substitute for them. Similar to HER, the overpotential and Tafel slope are two important indicators for the evaluation of OER catalytic performance. Table 2 lists the OER catalytic activity of some transition metal nitrides and noble metal catalysts.<sup>75</sup>

Single-metal nitride as non-noble metal catalyst has been studied for OER. Ni<sub>3</sub>N nanosheets have excellent OER catalytic performance in alkaline electrolyte. When the current density is 52.3 mA cm<sup>-2</sup>, the overpotential of Ni<sub>3</sub>N nanosheets is 350 mV and the Tafel slope is low.<sup>76</sup> It is worth noting that TMNs can be self-oxidized to corresponding metal oxides or hydroxides at the OER potential, which may enhance OER catalytic activity, and thus TMNs sometimes are called “precatalysts”.<sup>77</sup> Kawashima *et al.* reported that the Ni<sub>3</sub>N electrode self-oxidized into layered nickel hydroxides Ni(OH)<sub>2</sub> and NiOOH during the OER test,<sup>78</sup> which can facilitate the OER process. Fig. 8a and b show the enlarged and unamplified XRD patterns of nickel nitride/nickel foam before OER catalytic test. Fig. 8c and d show XRD patterns of nickel nitride/nickel foam

(NF) after multiple OER catalytic tests. It can be found that there is no new self-oxide crystal phase before OER, and amorphous oxides are formed on the surface after multiple OER tests. Ni<sub>3</sub>N is a metal conductor, NiOOH is a semiconductor, and Ni(OH)<sub>2</sub> is an insulator, which may cause the conductivity of Ni<sub>3</sub>N to decrease after multiple cycles (50–500 cycles), and the decrease of OER catalytic performance caused by the decrease of conductivity is greater than the increase of ECSA (electrochemical active area). However, doping a small amount of Fe in the catalyst can improve the conductivities of NiOOH and Ni(OH)<sub>2</sub>, and accordingly improve OER catalytic performance.<sup>79</sup> However, the real catalytic active sites of nickel nitride/nickel foam in the OER process remain to be investigated. OER in acidic solution is a bottleneck reaction. Most of the acidic OER catalysts are limited to IrO<sub>x</sub> catalysts, because IrO<sub>x</sub> is one of the catalysts that can balance activity and stability.<sup>80,81</sup> A future research direction could be to develop stable transition metal nitride OER catalysts with high OER activity in acidic electrolytes.

The bimetallic nitrides also have a wide range of applications in OER. By introducing secondary metals to TMNs, the electronic structure of the active site can be effectively regulated, the e<sub>g</sub> orbit of the active center and O 2p  $\sigma$  orbit of the reactant OH can be slightly overlapped, the transfer of charge carriers can be accelerated, and abundant lattice distortion can be formed, which all are conducive to OER.<sup>82</sup> An *et al.* prepared bimetallic Co<sub>0.15</sub>Fe<sub>0.85</sub>N<sub>0.5</sub> by the hydrothermal method.<sup>83</sup> Because the electronegativity of Fe is weaker than that of Co, it contributes to the expansion of the Fe–N bond and increases the degree of disorder. Co<sub>0.15</sub>Fe<sub>0.85</sub>N<sub>0.5</sub> shows a low overpotential (266 mV) at a current density of 10 mA cm<sup>-2</sup>, and the Tafel slope of OER is 30 mV dec<sup>-1</sup>, indicating that it has good OER catalytic activity. Liu *et al.* synthesized bimetallic nitrides with different Fe and Co ratios, such as CoFe (1 : 1)-N, CoFe(1 : 3)-N, CoFe(3 : 1)-N.<sup>84</sup> The CoFe(3 : 1)-N exhibits the best OER catalytic activity as shown in Fig. 8e. In 1.0 M KOH, when the driving current density is 10 mA cm<sup>-2</sup>, the overpotential of CoFe(3 : 1)-N is only 200 mV, which is lower than those of CoFe(1 : 1)-N, CoFe(1 : 3)-N and Co<sub>3</sub>N, and is even lower than that of RuO<sub>2</sub> (260 mV). The Tafel plot (Fig. 8f) also shows that the CoFe(3 : 1)-N has better OER catalytic activity than other samples. In addition, compared with other doping metals (Ni, Mn, Zn), Fe doping can make CoN exhibit better catalytic activity. As shown in Fig. 8g, h and i, the OER catalytic activity of CoFe(3 : 1)-N is higher than those of CoNi(3 : 1)-N, CoMn(3 : 1)-N and CoZn (3 : 1)-N. This is because the Lewis acid effect of Fe<sup>3+</sup> can promote the formation of Co<sup>4+</sup> active sites, which gives Fe<sup>3+</sup> advantages over other doped transition metals.

Porous carbon has good electrical conductivity and large specific surface area, and the coupling between carbonaceous materials and metal nitrides can create a synergistic effect, which can realize higher stability and activity. This synergistic effect is generally believed to be caused by the bridging effect between metal ions and active sites. The bridging effect between metal ions and carbon can modify oxygen-containing

**Table 2** The OER catalytic performance comparisons of various TMNs and RuO<sub>2</sub> catalysts

Material	Electrolyte	$\eta_{10}$ (mV)	Tafel slope (mV dec <sup>-1</sup> )	Ref.
2D-NCFe <sub>2</sub> Ni <sub>2</sub> N/rGO NHSS	0.1 M KOH	290	49.1	119
Ni <sub>3</sub> FeN	0.1 M KOH	335	72.9	119
VN/CNT/IF	1.0 M KOH	270	60	87
Ni <sub>3</sub> N NC	1.0 M KOH	190	56	121
Fe <sub>3</sub> N-CN	1.0 M KOH	218	47	122
Fe <sub>3</sub> N-M	1.0 M KOH	193	84	122
N <sub>1</sub> -CoS <sub>2</sub> -400	1.0 M KOH	285	93	123
Ni <sub>3</sub> N@Fe <sub>3</sub> N/CF-6	1.0 M KOH	294	40	124
Ce <sub>0.2</sub> -IrO <sub>2</sub> @NPC	0.5 M H <sub>2</sub> SO <sub>4</sub>	224	55.9	125
Co <sub>3</sub> N <sub>0.67</sub>	1.0 M KOH	258	52.22	126
RuO <sub>2</sub> /IF	1.0 M KOH	348	105	87

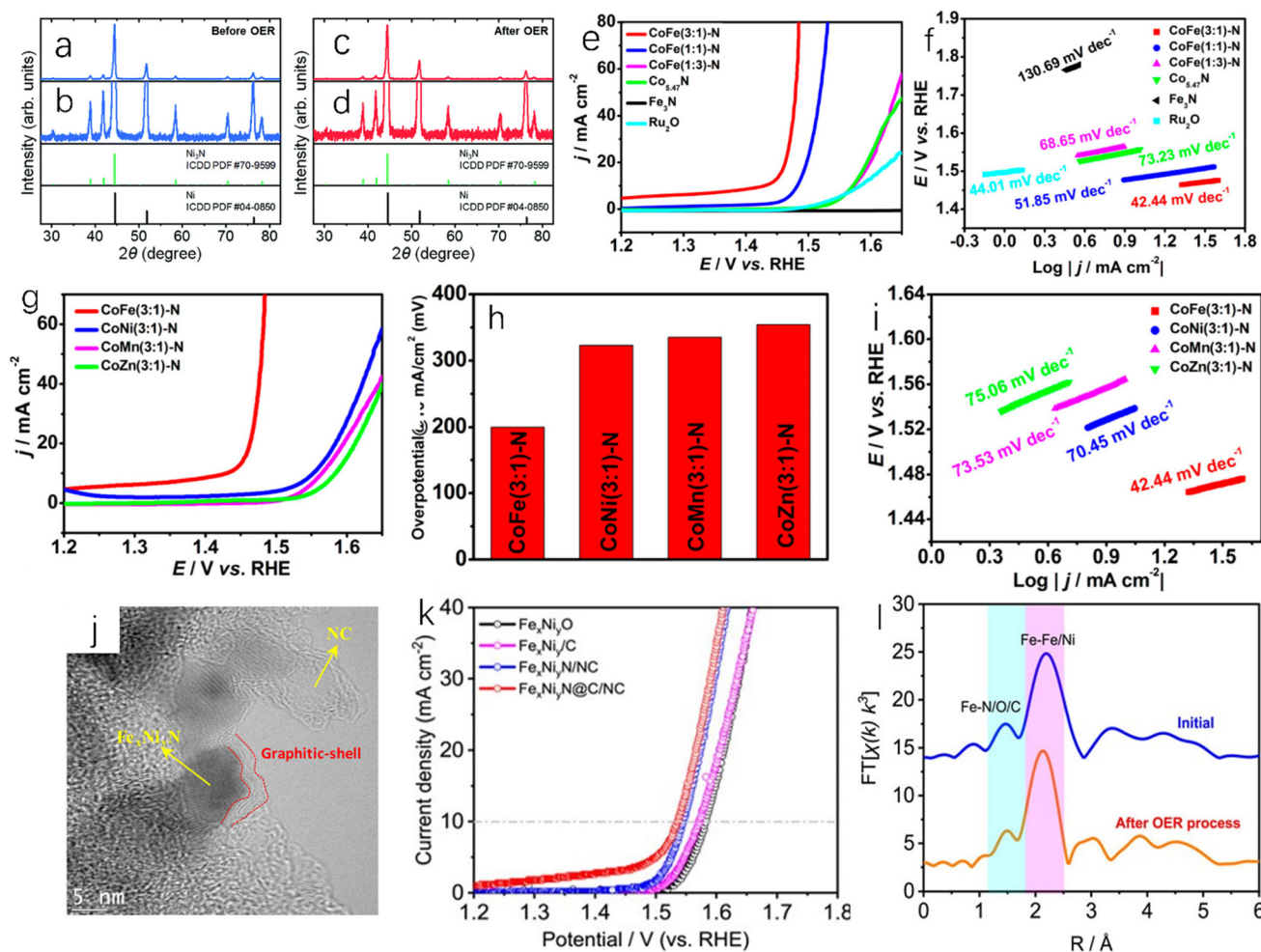


**Fig. 8** (a and b) XRD patterns of  $\text{Ni}_3\text{N}/\text{Ni}$  foam electrodes in 1.0 M KOH aqueous electrolyte; (c and d) XRD patterns of  $\text{Ni}_3\text{N}$  before and after OER 1000 cycles (0.25–0.75 V vs. Hg/HgO).<sup>78</sup> Copyright 2021, Royal Society of Chemistry; (e) record 100%  $iR$ -compensated linear sweep voltammetry (LSV) curve of OER at  $5 \text{ mV s}^{-1}$ ; (f) the Tafel slopes obtained from LSV curves in (e); (g) LSV polarization curves of different  $\text{CoM}(3:1)\text{-N}$  ( $M = \text{Fe, Ni, Mn, Zn}$ ) catalysts; (h) overpotentials of various catalysts at  $10 \text{ mA cm}^{-2}$ ; (i) Tafel plots of corresponding polarization curves.<sup>84</sup> Copyright 2018, American Chemical Society. (j) TEM image of  $\text{Fe}_x\text{Ni}_y\text{N}@C/\text{NC}$  catalyst; (k) polarization diagrams of  $\text{Fe}_x\text{Ni}_y\text{N}@C/\text{NC}$ ,  $\text{Fe}_x\text{Ni}_y/\text{NC}$ ,  $\text{Fe}_x\text{Ni}_y/\text{C}$  and  $\text{Fe}_x\text{Ni}_y\text{O}$  in  $\text{O}_2$ -saturated 1.0 M KOH at 1600 rpm; (l) the Fourier transforms of Fe K-edge extended X-ray absorption fine structure oscillations  $k^3\chi(k)$  of  $\text{Fe}_x\text{Ni}_y\text{N}@C/\text{NC}$  before and after OER process ( $k$ -weight: 3).<sup>86</sup> Copyright 2021, Wiley-VCH.

functional groups to enhance the coupling of heterogeneous species and form the related channels to accelerate electron transfer. In addition, the stability of  $\text{O}^*$  intermediates in carbon materials is an important factor affecting OER catalytic activity, and  $\text{O}^*$  intermediates can form bonds with carbon, which can improve the stability of  $\text{O}^*$  intermediates.<sup>85,129,130</sup> Wu *et al.* reported ternary  $\text{FeNi}$  alloy/nitride nanocrystals and graphitized shell and biomass-derived nitrogen-doped carbon ( $\text{Fe}_x\text{Ni}_y\text{N}@C/\text{NC}$ ).<sup>86</sup> As shown in Fig. 8j,  $\text{Fe}_x\text{Ni}_y\text{N}$  particles are covered by a thin layer of graphite, which makes it difficult for them to agglomerate or fall off under high oxidation conditions and can maintain high catalytic stability. Fig. 8k shows that the overpotential of  $\text{Fe}_x\text{Ni}_y\text{N}@C/\text{NC}$  (305 mV) is lower than those of  $\text{Fe}_x\text{Ni}_y/\text{NC}$  (315 mV),  $\text{Fe}_x\text{Ni}_y/\text{C}$  (341 mV) and  $\text{Fe}_x\text{Ni}_y\text{O}$  (353 mV) at a current density of  $10 \text{ mA cm}^{-2}$ . Due to the formation of  $\text{FeNi}$  nitride, the OER catalytic performance

of  $\text{Fe}_x\text{Ni}_y\text{N}@C/\text{NC}$  is greatly improved compared with  $\text{Fe}_x\text{Ni}_y/\text{C}$  and  $\text{Fe}_x\text{Ni}_y\text{O}$ . As shown in Fig. 8l, the bond combination of Fe did not change after OER, which was due to the fact that  $\text{Fe}_x\text{Ni}_y\text{N}$  nanocrystals encapsulated by the graphite shell were protected during the OER process and could maintain stability for more than 400 h at  $5.0 \text{ mA cm}^{-2}$ . Zhou *et al.* synthesized VN/CNT/IF by *in situ* growth of vertical VN nanoarray and carbon nanotube materials on iron foams.<sup>87</sup> As shown in Fig. 9a, VN/CNT/IF exhibits excellent OER catalytic activity, which is due to the fact that the nanotube structure exposes a large number of active sites that will let the electrode fully contact with the electrolyte. In industrial production, the catalyst needs to have high stability and activity at a high current density ( $1000 \text{ mA cm}^{-2}$ ). In 30 wt% KOH electrolyte (alkaline electrolyte is usually utilized in industrial production), the OER overpotential of VN/CNT/IF at a current density of



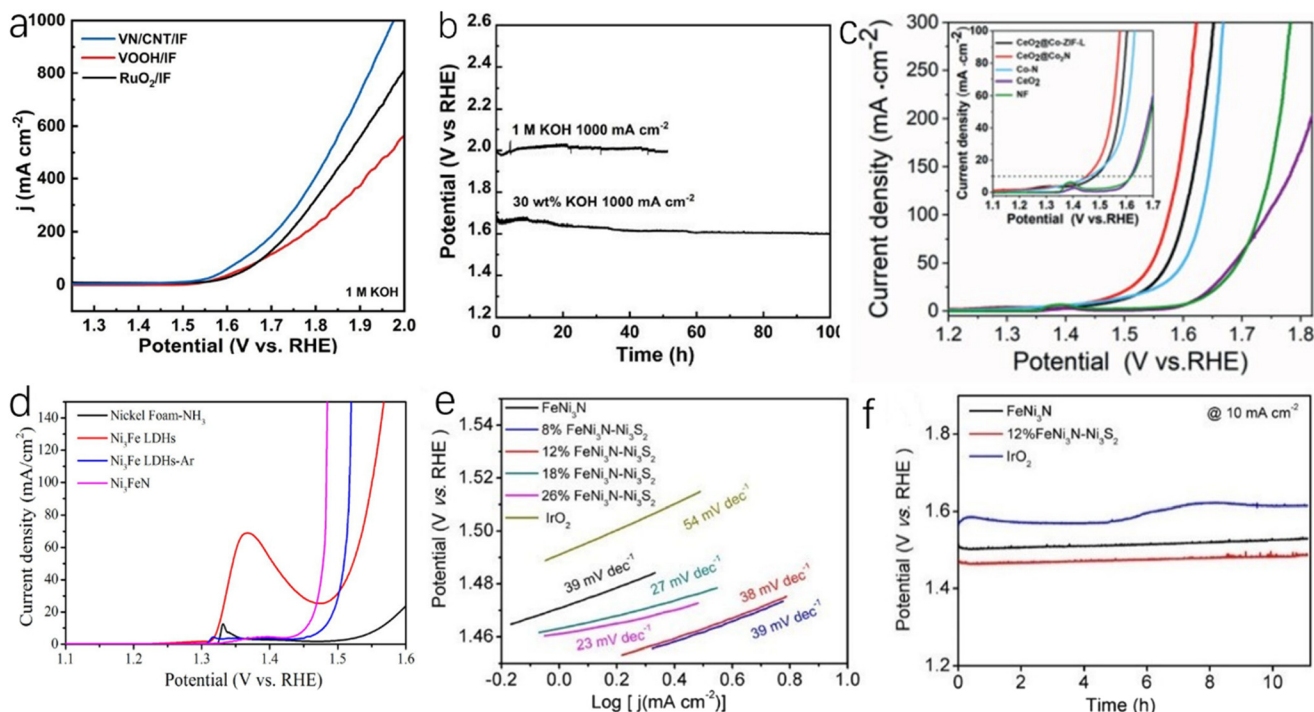


**Fig. 9** (a) LSV curves of RuO<sub>2</sub>/IF, VOOH/IF and VN/CNT/IF tested without *iR* compensation in 1.0 M KOH aqueous electrolyte; (b) chronopotentiometric curves of VN/CNT/IF in 30 wt% KOH electrolyte.<sup>87</sup> Copyright 2022, American Chemical Society; (c) LSV curves of CeO<sub>2</sub>@Co<sub>2</sub>N, CeO<sub>2</sub>@Co-ZIF-L, Co-N, CeO<sub>2</sub> and Ni foams in 1 M KOH electrolyte.<sup>88</sup> Copyright 2021, Wiley-VCH; (d) LSV curves of OER measured by nickel foam-NH<sub>3</sub>, Ni<sub>3</sub>Fe LDHs, Ni<sub>3</sub>Fe LDHs-Ar and Ni<sub>3</sub>FeN.<sup>89</sup> Copyright 2016, American Chemical Society; (e) Tafel slopes of FeNi<sub>3</sub>N-Ni<sub>3</sub>S<sub>2</sub>, FeNi<sub>3</sub>N and IrO<sub>2</sub> catalysts; (f) the current response of FeNi<sub>3</sub>N-Ni<sub>3</sub>S<sub>2</sub>, FeNi<sub>3</sub>N and IrO<sub>2</sub> catalysts measured chronoamperometrically at 10 mA cm<sup>-2</sup> within 40000 s.<sup>90</sup> Copyright 2020, American Chemical Society.

1000 mA cm<sup>-2</sup> is 410 mV. As shown in Fig. 9b, after 50 hours of testing, there was no significant degradation in OER catalytic performance.

Some metal nitride-related composite catalysts are also widely utilized for OER. Zhang *et al.* synthesized nanostructured Co<sub>2</sub>N@CeO<sub>2</sub> composites by using the self-template effect of zeolite imidazolate framework (ZIF).<sup>88</sup> This unique composite can provide a large number of active sites. As shown in Fig. 9c, the OER overpotential of Co<sub>2</sub>N@CeO<sub>2</sub> is 19 mV at a current density of 10 mA cm<sup>-2</sup>, and the OER catalytic performance at the same current density is significantly higher than other catalysts.<sup>88</sup> Wang *et al.* synthesized nanoparticle-stacked porous Ni<sub>3</sub>FeN (NSP-Ni<sub>3</sub>FeN) by using layered hydroxides (LDHs) of iron and nickel.<sup>89</sup> The catalyst retains the layered structure of LDHs, which can full expose active sites. As shown in Fig. 9d, the overpotential of NSP-Ni<sub>3</sub>FeN for OER is only 223 mV at a current density of 10 mA cm<sup>-2</sup>. Liang *et al.* obtained a nitride-sulfide composite (FeNi<sub>3</sub>N-Ni<sub>3</sub>S<sub>2</sub>) catalyst by the hydrothermal method.<sup>90</sup> As shown in Fig. 9e, the Tafel slope of FeNi<sub>3</sub>N-Ni<sub>3</sub>S<sub>2</sub> (12 wt%) (Ni<sub>3</sub>S<sub>2</sub> content is 12 wt%) is 38 mV dec<sup>-1</sup>, which is much smaller than the Tafel slopes of FeNi<sub>3</sub>N and IrO<sub>2</sub>, and the overpotential is only 230 mV at a current density of 10 mA cm<sup>-2</sup>, which is smaller than the overpotential of FeNi<sub>3</sub>N under the same conditions (270 mV). The OER catalytic performance of FeNi<sub>3</sub>N-Ni<sub>3</sub>S<sub>2</sub> has been greatly

improved compared with FeNi<sub>3</sub>N. As shown in Fig. 9f, the potential of IrO<sub>2</sub> increased significantly after 6 hours of testing, while the potential of FeNi<sub>3</sub>N-Ni<sub>3</sub>S<sub>2</sub> did not change significantly after 11 hours of testing, and the stability of FeNi<sub>3</sub>N-Ni<sub>3</sub>S<sub>2</sub> was obviously higher than that of IrO<sub>2</sub>. The Co-based anti-perovskite nitride CuNC<sub>3-x</sub>V<sub>x</sub> (0 ≤ x ≤ 1) reported by Zhang *et al.* showed excellent catalytic activity and stability for OER.<sup>91</sup> Compared with traditional Ir/C, the CuNC<sub>3-x</sub>V<sub>x</sub> shows a current density of 10 mA cm<sup>-2</sup> at an overpotential of 235 mV, which is similar to Ir/C, but the stability of Ir/C is much lower than that of CuNC<sub>3-x</sub>V<sub>x</sub>. The anti-perovskite structure makes ANCo<sub>3</sub> (A: transition metal) tunable, which can provide the potential for optimizing electrocatalytic performance.<sup>92</sup>

In summary, as one of the alternatives to precious metal catalysts for OER, the transition metal nitrides have attracted much attention due to their excellent activity and stability. At present, many studies have shown that the OER catalytic activities of transition metal nitrides are comparable to those of noble metal catalysts under experimental conditions. However, their catalytic activities and long-term stabilities at a high current density are unsatisfactory, and they still cannot replace the noble metals in OER applications. In addition, although some studies have found that the surface oxidation of TMNs is beneficial for OER, whether this oxidation is really beneficial

**Table 3** The ORR catalytic performance comparisons of various TMNs and Pt/C catalysts

Material	Electrolyte	Initial potential (V)	Half-wave potential (V)	Limiting current density ( $\text{mA cm}^{-2}$ )	Tafel slope ( $\text{mV dec}^{-1}$ )	Ref.
$\text{Ni}_{2.25}\text{Co}_{0.75}\text{N}/\text{NrGO-3}$	0.1 M KOH	0.874	0.79	5.35	56	120
$\text{Ni}_{2.25}\text{Co}_{0.75}\text{N}$	0.1 M KOH	—	0.538	3.11	65	120
$\text{Ti}_{0.8}\text{Co}_{0.2}\text{N}$	0.1 M $\text{HClO}_4$	0.96	0.79	5.65	—	102
$\text{NiFe}_3@\text{NGHS-NCNTs}$	0.1 M KOH	0.97	0.823	5.68	99.4	106
$\text{Fe}@\text{NGHS-NCNTs}$	0.1 M KOH	0.95	0.843	5.83	107.21	106
$\text{NiFe}_3@\text{NGHS-NCNTs}$ (thick)	0.1 M KOH	0.95	0.818	6.33	110.29	106
$\text{Pt}/\text{Ti}_3\text{C}_2\text{T}_x$	0.1 M KOH	0.95	—	6.5	—	127
Pt/C	0.1 M KOH	0.998	0.87	5.34	80	120

remains to be studied. At present, most of the research is devoted to the application of TMNs in alkaline electrolytes, while ignoring the catalytic activity and stability in acidic electrolytes. In the future, OER catalysts based on TMNs in acidic electrolyte could be considered.<sup>77</sup>

### 4.3 Application in oxygen reduction reaction

The oxygen reduction reaction (ORR) is the cathode reaction of the fuel cell, and is divided into a two-electron reaction and four-electron reaction. Because  $\text{H}_2\text{O}_2$  can poison fuel cells, it is more advantageous to directly conduct a four-electron reaction. The research direction of an ORR catalyst is to promote ORR to be a four-electron process. The intermediate product of ORR with two-electron pathway is  $\text{H}_2\text{O}_2$ , which can be used as a synthesis method of hydrogen peroxide. The four-electron reaction is often restricted by d electrons. Some transition metals have the problem of insufficient d electrons, which makes them unable to support efficient ORR reactions. Therefore, increasing the d electrons of a transition metal is an effective strategy to enhance the ORR catalytic activity of TMNs.<sup>9</sup> A variety of transition metal nitrides have been studied for ORR. Table 3 lists the ORR catalytic activities of some TMNs and precious metal catalysts.

At present, transition metal nitrides as catalysts for ORR mainly have three limitations, namely, insufficient d electrons, low exposure of active sites and low conductivity. Especially for single-metal nitrides, their ORR catalytic activity is much lower than that of commercial Pt/C catalysts.<sup>93</sup> However, under certain conditions, single-metal nitrides show high ORR catalytic activity. Kreider *et al.* prepared nickel nitride films and measured the ORR catalytic activity and selectivity of  $\text{Ni}_x\text{N}$  in acidic (0.1 M perchloric acid) and alkaline electrolytes (0.1 M potassium hydroxide).<sup>94</sup> As shown in Fig. 10a and b, nickel nitride shows excellent ORR catalytic activity in an acidic environment. The onset potential of ORR is 0.68 V (vs. RHE, the same below) at  $100 \mu\text{A cm}^{-2}$ , the mass transfer control current density is  $6.1 \text{ mA cm}^{-2}$  at 0.2 V, the half-wave potential is 0.49 V, and the Tafel slope is  $89.7 \text{ mV dec}^{-1}$ . However, the catalytic activity of  $\text{Ni}_x\text{N}$  under alkaline conditions is poorer than that in acid. The initial potential is 0.68 V, but its mass transfer control current density is only  $4 \text{ mA cm}^{-2}$ , the half-wave potential is 0.42 V, and the Tafel slope is  $175 \text{ mV dec}^{-1}$ . Under alkaline conditions, nickel nitride has a high selectivity

to  $\text{H}_2\text{O}_2$ , while under acidic conditions, the selectivity of ORR to  $\text{H}_2\text{O}_2$  decreases with increasing potential (Fig. 10c). Huang *et al.* synthesized nano-VN with hexagonal structure by hydrothermal method (Fig. 10d).<sup>95</sup> As shown in Fig. 10e and f, VN has excellent ORR activity in 1.0 M KOH. The onset potential of VN is only  $-0.14 \text{ V}$ , close to that of Pt ( $-0.04 \text{ V}$ ), indicating great potential for VN as a catalyst for ORR. The Tafel slope of VN ( $69.13 \text{ mV dec}^{-1}$ ) is similar to that of Pt ( $69.22 \text{ mV dec}^{-1}$ ) as shown in Fig. 10g. However, it is worth noting that, similar to OER, TMNs are inevitably oxidized to varying degrees in ORR, which has an impact on the activity and selectivity of TMNs. Whether this effect is beneficial or not has not been determined. Kreider *et al.*<sup>96</sup> reported the effect of O incorporation on the ORR activity and selectivity of TiN. The rotating ring-disc electrode (RRDE) was used to separate the contribution of the four-electron pathway and the two-electron pathway to the total catalytic activity in 0.1 M  $\text{HClO}_4$ . As shown in Fig. 10h and i, the total current and 4e-current of MoN are greater than those of MoNO and  $\text{MoNO}_{1-x}$ , but the selectivity of MoN to the two-electron pathway is low. At 0.3 V vs. RHE,  $\text{MoNO}_{1-x}$  has a  $\text{H}_2\text{O}_2$  selectivity of 65–80% and partial  $\text{H}_2\text{O}_2$  current density of  $0.63\text{--}0.88 \text{ mA cm}^{-2}$ , and MoN ( $\text{H}_2\text{O}_2$  selectivity of 21–60%, partial current density of  $0.31\text{--}0.95 \text{ mA cm}^{-2}$ ) has a wide 2e activity range. By comparing the electrochemical double-layer capacitance (EDLC), as shown in Fig. 10j, it can be found the order is  $\text{Mo}_2\text{NO} > \text{MoN} > \text{MoNO}_{1-x}$ , which shows that MoNO has a higher electrochemical active area.

In metal nitrogen oxides, an increase in nitrogen content will increase the lattice constant, the occupancy of anionic sites and the valence of metals, thereby improving the catalytic activity of ORR. Miura *et al.* reported the effect of the proportion of nitrogen in metal nitrogen oxides on the activity,<sup>97</sup> and the results showed that the sample MnON(2) had highest nitrogen content, followed by MnON(3) and MnON(1). The Mn/O/N molar ratios were 1:0.24:0.84 in MnON(1), 1:0.19:0.78 in MnON(2), and 1:0.19:0.64 in MnON(3). The experimental results showed that the increasing of nitrogen content reduced the overpotential of ORR and could promote the four-electron pathway, as shown in Fig. 10k.<sup>97</sup> The increase of nitrogen content makes the onset potential move to high potential direction. The samples MnON(1) and MnON(2) both had high electrocatalytic activity of ORR. According to the Koutecký–Levich diagram (Fig. 10l), the electron number of MnON(1),

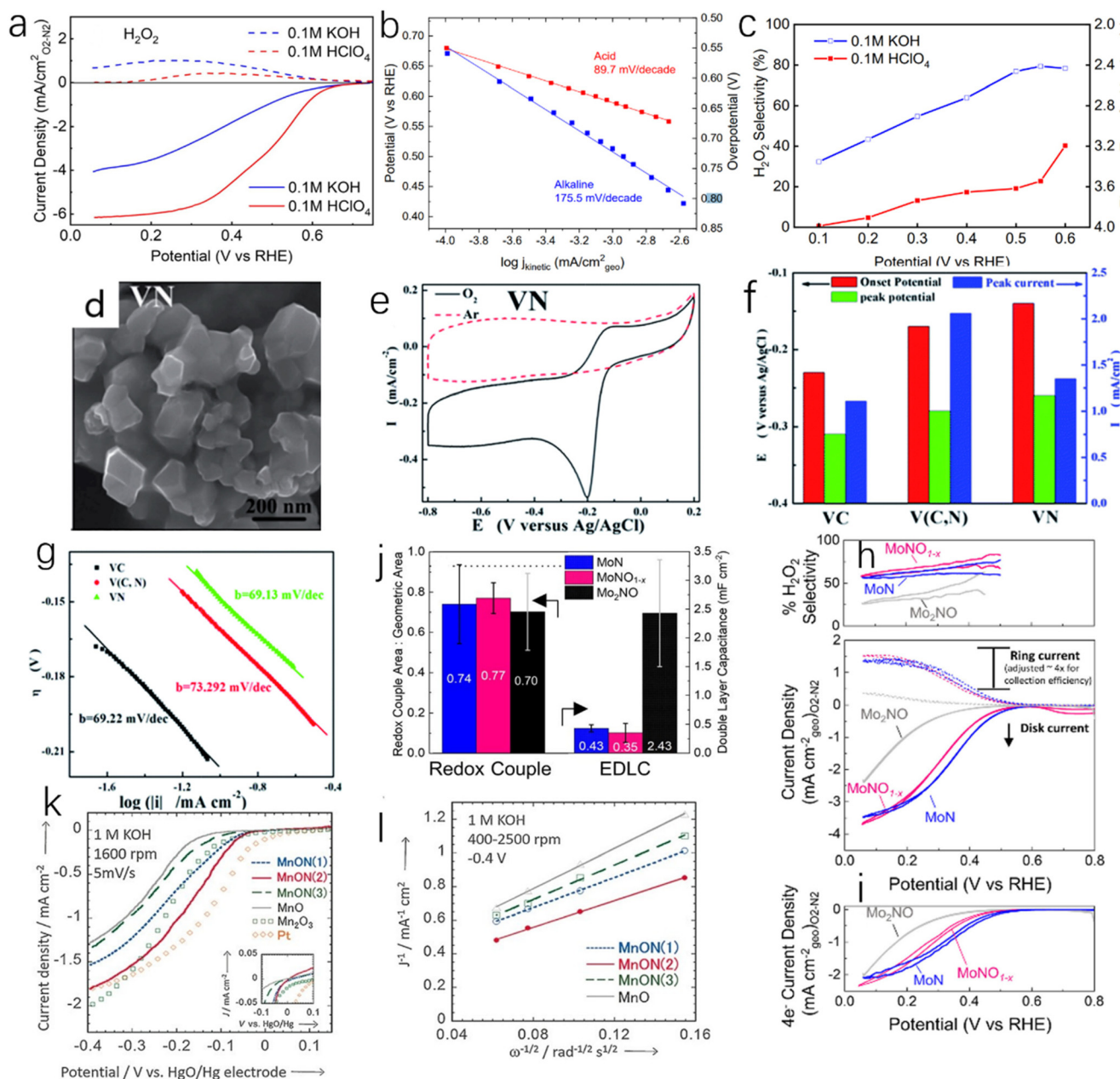


**Fig. 10** (a) LSV curves of  $\text{Ni}_x\text{N}$  in acid (red) and alkali (blue); (b) Tafel slope curves of nickel nitride in acidic (red) and alkaline (blue) electrolytes; (c)  $\text{H}_2\text{O}_2$  selectivity and electron transfer number of nickel nitride under acidic and alkaline conditions.<sup>94</sup> Copyright 2019, American Chemical Society; (d) SEM image of VN; (e) cyclic voltammetry test of VN for ORR performed at a scan rate of  $0.01 \text{ V s}^{-1}$  in argon and oxygen-saturated electrolytes, respectively; (f) the onset potential, peak potential and peak current of VN, V(C, N) and VC catalyzed ORR at a scan rate of  $0.05 \text{ V s}^{-1}$ ; (g) Tafel slopes of VN, V(C, N) and VC catalysts at  $0.005 \text{ V s}^{-1}$ .<sup>95</sup> Copyright 2014, Royal Society of Chemistry; (h) LSV curves measured with total current density (geometric basis) from the disk and the ring (Pt ring adjusts the collection efficiency,  $\sim 4\times$ ) and the corresponding  $\text{H}_2\text{O}_2$  selectivity, as measured by RRDE; (i) LSV curves measured with  $4e^-$  current density (geometry); (j) the fraction of the geometric area calculated by EDLC of the three catalysts.<sup>96</sup> Copyright 2020, American Chemical Society; (k) the LSV curves of MnON(1), MnON(2), MnON(3) and MnO in  $\text{O}_2$ -saturated 1.0 M KOH solution recorded by rotating disk electrode at a scan rate of  $5 \text{ mV s}^{-1}$ . The LSV curves of Pt/C and  $\text{Mn}_2\text{O}_3$  were compared; (l) Koutecký–Levich curves measured at  $-0.4 \text{ eV}$  and 400–2500 rpm.<sup>97</sup> Copyright 2016, Wiley-VCH.

MnON(2) and MnON (3) is 3.2, 3.6 and 3.8, respectively, indicating that the increase in nitrogen content can reduce the overpotential of ORR and promote the four-electron pathway. The formation of bulk metal nitrogen oxides is beneficial for ORR, due to the strong driving force of O infiltration on the  $\text{Mo}_2\text{N}$  struc-

ture. For the perovskite oxides, the covalent nature of metal–oxygen bonds is conducive to ORR. The electronic structure of oxynitrides with rock salt-like structure is similar to that of the perovskite oxides, which means that the role of metal–oxygen bonds will increase ORR catalytic activity.<sup>98</sup>



Iron group transition metal nitrides such as Co and Fe nitrides have excellent ORR activity under alkaline conditions, but they are not stable under acidic conditions.<sup>99</sup> Some transition metal nitrides are stable at low pH and show high ORR catalytic activity. Doping secondary metals can make TMNs exhibit excellent ORR performance and stability under alkaline and acidic conditions. It was found that doping secondary metals with rich d electrons can increase d electrons of the catalyst, which can improve ORR catalytic performance.<sup>93</sup> Fritz *et al.* reported the doping of secondary metals in MoN (such as  $\text{Fe}_{0.8}\text{Mo}_{1.2}\text{N}_2$ ,  $\text{Co}_{0.6}\text{Mo}_{1.4}\text{N}_2$ , and  $\text{MnMoN}_2$ ).<sup>100</sup> As shown in Fig. 11a, the ORR catalytic activities of  $\text{Fe}_{0.8}\text{Mo}_{1.2}\text{N}_2$  ( $5.3 \mu\text{A cm}_{\text{catalyst}}^{-2}$ ) and  $\text{Co}_{0.6}\text{Mo}_{1.4}\text{N}_2$  ( $11.6 \mu\text{A cm}_{\text{catalyst}}^{-2}$ ) are higher than that of  $\text{Mo}_2\text{N}$ , but the activity of  $\text{MnMoN}_2$  ( $1.4 \mu\text{A cm}_{\text{catalyst}}^{-2}$ ) is lower than that of  $\text{Mo}_2\text{N}$ . It can be found that doping different secondary metal into TMNs will have

different effects on ORR catalytic performance. Cao *et al.* reported the ORR catalytic performance of Co-doped MoN ( $\text{Co}_{0.6}\text{Mo}_{1.4}\text{N}_2$ ).<sup>101</sup> By analyzing rotation rate dependence of the rotating disk electrode (RDE) data, as shown in Fig. 11b, under acidic conditions (0.1 M  $\text{HClO}_4$ ), it was found that the four-electron process is dominant below 0.50 V, while the two-electron process coexists with the four-electron process above 0.50 V. At all potentials, the current density of  $\text{Co}_{0.6}\text{Mo}_{1.4}\text{N}_2$  is greater than that of MoN (Fig. 11c). The enhanced ORR electrocatalytic performance of molybdenum nitride after Co doping may be due to the changes of surface morphology and electronic structure caused by Co substitution. Tian *et al.* found that the ORR catalytic activity of the binary metal nitrides obtained by doping TiN with Co was significantly improved (in 0.1 M  $\text{HClO}_4$ ),<sup>102</sup> and  $\text{Ti}_{0.8}\text{Co}_{0.2}\text{N}$  shows the best ORR catalytic performance (Fig. 11d). The onset potential and half-wave

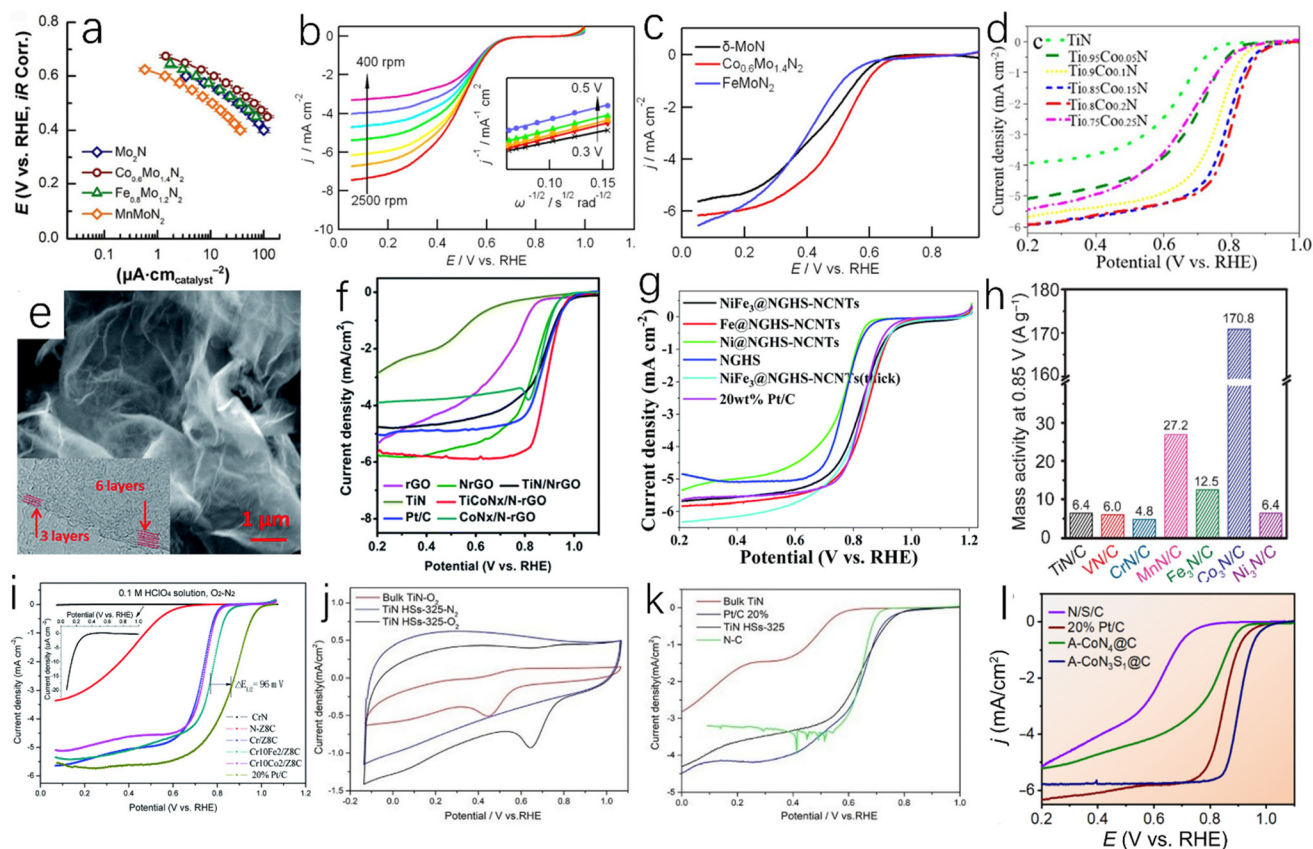


**Fig. 11** (a) The ORR specific activity of molybdenum-based catalysts normalized by BET specific surface area.<sup>100</sup> Copyright 2019, Springer Link; (b) RDE curves of  $\text{Co}_{0.6}\text{Mo}_{1.4}\text{N}_2$  at 400–2500 rpm and the corresponding to Koutecký–Levich plot (inset) (potential range is 0.30–0.50 V vs. RHE); (c) RDE curves of  $\delta\text{-MoN}$ ,  $\text{Co}_{0.6}\text{Mo}_{1.4}\text{N}_2$  and  $\text{FeMoN}_2$ .<sup>101</sup> Copyright 2015, American Chemical Society; (d) LSV curves of  $\text{Ti}_{1-x}\text{Co}_x\text{N}$  with different Co doping concentrations.<sup>102</sup> Copyright 2018, American Chemical Society; (e) SEM and TEM images of graphene oxide; (f) LSV curves of rGO, N-rGO,  $\text{TiN/N-rGO}$ ,  $\text{TiCoN}_x/\text{N-rGO}$ ,  $\text{CoN}_x/\text{N-rGO}$ ,  $\text{TiN}$  and  $\text{Pt/C}$  for ORR.<sup>105</sup> Copyright 2017, Royal Society of Chemistry; (g) LSV curves of  $\text{NiFe}_3@\text{NGHS-NCNTs}$ ,  $\text{Fe}@\text{NGHS-NCNTs}$ ,  $\text{Ni}@\text{NGHS-NCNTs}$ ,  $\text{NGHS}$ ,  $\text{NiFe}_3@\text{NGHS-NCNTs}$  (thick) and 20 wt%  $\text{Pt/C}$  for ORR in  $\text{O}_2$ -saturated 0.1 M KOH.<sup>106</sup> Copyright 2022, Royal Society of Chemistry; (h) comparison of mass activities of various  $\text{M}_x\text{N/C}$  catalysts measured at 0.85 V.<sup>107</sup> Copyright 2022, Science; (i) LSV curves of  $\text{CrN}$ ,  $\text{N-Cr}_6\text{C}$ ,  $\text{Cr/ZrC}$ ,  $\text{Cr}_{10}\text{Fe}_2/\text{ZrC}$ ,  $\text{Cr}_{10}\text{Co}_2/\text{ZrC}$  and JM 20 wt%  $\text{Pt/C}$  in 0.1 M  $\text{HClO}_4$  solution.<sup>109</sup> Copyright 2020, Royal Society of Chemistry; (j) CV curves of  $\text{TiN HSS-325}$  and bulk  $\text{TiN}$  in 0.1 M KOH saturated with  $\text{N}_2$  and  $\text{O}_2$  at a scan rate of  $50 \text{ mV s}^{-1}$ ; (k) RDE voltammograms of  $\text{TiN HSS}$ , bulk  $\text{TiN}$ ,  $\text{N-C}$  and  $\text{Pt/C}$  in  $\text{O}_2$ -saturated 0.1 M KOH at a scan rate of  $10 \text{ mV s}^{-1}$  and a rotation speed of 1600 rpm.<sup>111</sup> Copyright 2019, American Chemical Society. (l) LSV curves of  $\text{N/S/C}$ , 20 wt%  $\text{Pt/C}$ ,  $\text{A-CoN}@\text{N/S/C}$ ,  $\text{A-CoN}_4@\text{C}$  and  $\text{A-CoN}_3\text{S}_1@\text{C}$  catalysts at a rotation rate of 1600 rpm (scan rate:  $5 \text{ mV s}^{-1}$ ).<sup>143</sup> Copyright 2022, Springer Link.

potential were 0.96 V and 0.79 V, respectively, and the limiting density was  $5.65 \text{ mA cm}^{-2}$ . Doping with Co will cause the change of the Ti electronic structure, which is beneficial for improving the ORR activity of TiN. In addition to high ORR catalytic activity, the  $\text{Ti}_{0.8}\text{Co}_{0.2}\text{N}$  catalytic process is dominated by the four-electron pathway with low peroxide yield, which indicates that it can be applied to fuel cells to reduce the toxicity of the two-electron pathway to the battery, and the Co atom will be combined with the interstitial site of TiN, which makes  $\text{Ti}_{0.8}\text{Co}_{0.2}\text{N}$  extremely stable in an acidic electrolyte.

Compounding carbon materials with metal nitrides can increase the specific surface area of the catalyst, provide favorable adsorption sites for oxygen, and acquire the advantages of low cost, high catalytic activity and long-term stability.<sup>103</sup> The synergistic effect of carbon materials and transition metal nitrides in ORR is similar to that of OER, which can be explained by the bridging effect. Carbon materials make the active sites of transition metal nitrides have higher adsorption energy for oxygen-containing intermediates, thus having better ORR activity.<sup>130,131</sup> In addition, the multi-dimensional structure of carbon materials can confine the growth of alloy particles and avoid particle agglomeration.<sup>104</sup> Dong *et al.* synthesized TiN nanoparticles supported on N-doped reduced graphene oxide (NrGO).<sup>105</sup> The specific surface area of graphene oxide (GO) is  $469.4 \text{ m}^2 \text{ g}^{-1}$ , and the pore volume is  $1.07 \text{ cm}^3 \text{ g}^{-1}$ . The larger specific surface area and microstructure of GO (Fig. 11e) are conducive to the diffusion of reactants or intermediates. As shown in Fig. 11f, TiN exhibits poor ORR catalytic activity in 0.1 M KOH, while TiN/N-rGO shows high ORR catalytic activity with onset potential and half-wave potential of 0.961 and 0.872 V, respectively, which are much better than TiN and are even comparable to Pt/C catalyst. The  $\text{NiFe}_3\text{@NGHS-NCNTs}$  synthesized by Ma *et al.* also showed excellent ORR catalytic performance.<sup>106</sup> As shown in Fig. 11g, the limiting current density and half-wave potential of  $\text{NiFe}_3\text{NGHS-NCNTs}$  are  $5.68 \text{ mA cm}^{-2}$  and 0.97 V, respectively, which are comparable to Pt/C ( $5.66 \text{ mA cm}^{-2}$ , 0.829 V). Zeng *et al.* found that the  $\text{Co}_3\text{N/C}$  catalyst had excellent catalytic activity for ORR.<sup>107</sup> The mass activity (MA) of  $\text{Co}_3\text{N/C}$  was tested at 0.85 V vs. RHE and it was  $\sim 170 \text{ A g}^{-1}$  (Fig. 11h). The low conductivity of some metal nitrides, such as CrN and NbN, limits their applications for ORR. Another advantage of carbon materials is their high conductivity, which can be improved by compounding with these TMNs.<sup>108</sup> Luo *et al.* prepared CrN nanoparticles supported on ZIF-8-derived carbon (Cr/Z8C),<sup>109</sup> which could greatly enhance the conductivity of CrN. As shown in Fig. 11i, CrN showed poor ORR catalytic activity in acidic solutions, while CrN/Z8C showed high ORR catalytic activity (half-wave potential is 0.722 V). Among many M–N–C catalysts, Fe and Co nitrides exhibit high ORR performance, and their ORR catalytic activity is sometimes comparable even to that of commercial Pt/C catalyst.<sup>110</sup>

Some nanostructured metal nitride catalysts also exhibit good application prospects for ORR. Chen *et al.* prepared TiN hollow spheres (TiN HSS) assembled by 2D nanosheets using carbon as a template.<sup>111</sup> It was found that the temperature had

a certain effect on the catalytic performance of the product during the synthesis process. As shown in Fig. 11j and k, TiN HSS-325 (calcined at 325 °C during synthesis) showed excellent ORR catalytic activity. The onset and peak potentials of TiN HSS-325 were 0.83 and 0.68 V, respectively, which were higher than those of bulk TiN. The limiting current density of TiN HSS-325 was about  $4.5 \text{ mA cm}^{-2}$ . The above onset potential and limiting current density values are close to those of Pt/C catalyst. The high ORR catalytic activity of TiN HSS-325 is due to the increase in the exposed active sites. Jia *et al.* reported a 2D metal nitride of single-layer  $\text{RuN}_2$  with four-coordinated Ru atoms and isolated  $\text{N}=\text{N}$  dimers,<sup>112</sup> exhibiting a quite high ORR catalytic activity with high limiting potential (0.99 V) and selectivity for the four-electron pathway. Zhao *et al.* synthesized  $\text{NiN}_3\text{-BP}$  by combining TMNs with 2D black phosphorus (BP).<sup>113</sup> DFT calculation results show that the catalytic performance of  $\text{NiN}_3\text{-BP}$  is related to the number of doped nitrogen atoms around the metal, and the coordination of N atoms can well regulate the adsorption strength of the metal center on oxygen-containing intermediates, thereby regulating ORR catalytic performance. Because of the above advantages,  $\text{NiN}_3\text{-BP}$  exhibits high ORR catalytic activity (ORR overpotential is 0.44 V).<sup>113</sup> In fuel cells and air batteries, metal nitrides are often used as ORR electrocatalysts. Zhi *et al.* reported an  $\text{A-CoN}_3\text{S}_1\text{@C}$  electrocatalyst based on the atomic exchange strategy.<sup>143</sup> S doping can adjust the electronic structure of the catalytic active center to improve the electrocatalytic activity. As shown in Fig. 11l, the half-wave potential of  $\text{A-CoN}_3\text{S}_1\text{@C}$  in 1.0 M KOH is 0.91 V (vs. RHE), and the limiting current density is  $5.81 \text{ mA cm}^{-2}$ , with higher ORR activity than that of  $\text{A-CoN}_4\text{@C}$ . This indicates that doping with S and the  $\text{CoN}_3\text{S}_1$  part can improve ORR catalytic activity by regulating the electronic structure of Co.<sup>143</sup> The metal nitrides can enhance the ORR catalytic performance and iodine adsorption in zinc-iodine batteries, and the amorphous iron nitride structure can form abundant defects and provide more catalytic active sites, reducing the reaction polarization.<sup>144</sup>

Most fuel cells are expensive because the ORR reaction is slow and requires expensive Pt-based catalysts to reduce the overpotential. The high prices and susceptibility to poisoning of Pt-based catalysts have prevented their widespread applications for ORR. Therefore, the transition metal nitrides with low cost, high activity, high applicability and strong anti-toxicity exhibit good prospects for fuel cells.<sup>114</sup> In theory, TMNs have excellent ORR catalytic performance, but in practical applications for ORR, there are many problems, such as low conductivity, insufficient d electrons and low exposure of active sites. Currently, most studies have focused on increasing the number of d electrons in TMNs, such as doping transition metals with rich d electrons. However, in future studies, in addition to considering the number of d electrons, more efforts can also be made to improve the conductivity and active site number of TMNs.<sup>93</sup>

Among the various metal nitrides introduced above, metal nitrides and their related materials containing different transition metals such as molybdenum, nickel, cobalt, tungsten,

titanium, iron, copper, *etc.* are widely studied in HER. Transition metal nitrides and their related materials containing nickel, cobalt, manganese, iron, *etc.* are often used in OER. In ORR, transition metal nitrides and their related materials such as cobalt, iron, manganese, nickel, titanium, *etc.* are often used.<sup>134–136</sup> It can be found that the same transition metal nitride can be applied to different reactions, but their catalytic mechanisms are slightly different. For example, nickel nitride can be applied to the above three electrocatalytic reactions. Nickel nitride has active sites with small hydrogen adsorption energy, which indicates that nickel nitride has excellent HER activity. The overpotential of Ni<sub>3</sub>N nanosheets prepared by Gao *et al.*<sup>137</sup> at a current density of 10 mA cm<sup>-2</sup> is 59 mV, and the Tafel slope is 59.79 mV dec<sup>-1</sup>, which is similar to that of Pt, which is due to the smaller  $\Delta G_{\text{H}}$  on the N–Ni surface. Xu *et al.* found that Ni<sub>3</sub>N nanosheets have a disordered structure that leads to the reduced size,<sup>76</sup> which can provide more active sites for OER. When the current density is 52.3 mA cm<sup>-2</sup>, the overpotential is 350 mV, and the Tafel slope is 45 mV dec<sup>-1</sup>. In Ni<sub>3</sub>N, Ni is highly sensitive to the surface adsorption of molecular oxygen, which makes Ni<sub>3</sub>N have excellent ORR performance. The onset potential of Ni<sub>3</sub>N prepared by Kreider *et al.* was 0.68 V in both acidic electrolyte (0.1 M perchloric acid) and alkaline electrolyte (0.1 M potassium hydroxide).<sup>94</sup>

Compared with nickel nitride, the valence electron arrangement of Co is 3d<sup>7</sup>4s<sup>2</sup>, and the d orbital is not filled, which makes the anti-bonding state of Co close to the Fermi level (EF), and there are few empty orbitals, so it has good electron-donating ability. Han *et al.* prepared Co<sub>4</sub>N nanowires (Co<sub>4</sub>N NWS) and tested their catalytic performance for HER.<sup>138</sup> In 1.0 M KOH, the Tafel slope was 180 mV dec<sup>-1</sup>. The cobalt nitride nanowires prepared by Zhang *et al.* showed excellent OER catalytic performance in 1.0 M KOH electrolyte.<sup>139</sup> The overpotential was 10 mV at a current density of 290 mA cm<sup>-2</sup>, and the Tafel slope was 70 mV dec<sup>-1</sup>. Yang *et al.* reported that Co<sub>4</sub>N/C has excellent ORR activity with a half-wave potential of 0.875 V in 1.0 M KOH,<sup>140</sup> which is very close to that of the commercial Pt/C (0.89 V). For the application of metal nitrides in HER, OER and ORR, in addition to the difference in catalytic activity and catalytic mechanism, another major difference is that metal nitrides will inevitably be oxidized in OER and ORR, and this oxidation will change the active site and often enhance the catalytic activity.

## 5. Conclusions and perspectives

In this paper, various synthesis methods for metal nitride catalysts and their applications in the fields of HER, OER and ORR electrocatalysis are reviewed. Transition metal nitrides are similar to precious metals in structure, which makes them one of the alternatives to precious metals. TMNs have good corrosion resistance and high stability. Compared with metal oxides/hydroxides, TMNs have better conductivity. Compared with the original metal, the TMN has a larger specific surface

area to expose more active sites. Doping with other metals can form bimetallic nitrides, and the synergistic effect between different metals and the resulting changes in electronic structure contribute to the improvement of catalytic activity. However, it is worth noting that although transition metal nitrides have excellent catalytic activity in non-noble metal catalysts, there is still an obvious gap compared with noble metal catalysts. Future research may be carried out from the following aspects:

Firstly, metal nitrides in electrocatalytic reactions, especially OER and ORR, are easily oxidized to varying degrees, which can provide more active sites to improve the catalytic activity. However, the conductivities of metal oxides/nitrogen oxides formed by oxidation are not high, which will obviously reduce the electrocatalytic performance of TMNs over long cycles. Doping transition metals into metal oxides/nitrogen oxides can improve their conductivities. It is found that the metal doping can efficiently improve the catalytic activity and stability of the metal oxides/nitrogen oxides for OER and ORR. As we all know, the different oxidation degrees will lead to the different catalytic activities, so it is important to find the optimal oxidation degree corresponding to TMNs, or to prevent the oxidation of TMNs during the catalytic reactions. In addition, it is worth noting that it is uncertain whether this oxidation is beneficial in HER, and subsequent research needs to further explore the effect of metal nitride oxidation in HER.

Secondly, reasonable interface engineering design can adjust the active site density, charge transfer ability and mass transfer ability of the catalyst. Interface engineering design includes defect engineering, morphology engineering and heterogeneous interface engineering. Reasonable interface design can improve effective strategies for the synthesis of advanced transition metal nitrides. DFT calculations can explain the principle of the catalyst, the active site and the influence of various factors on the catalyst at the atomic level, and provide design strategies for the synthesis of more excellent catalysts.

Thirdly, at present, most single-phase metal nitride catalysts exhibit only one kind of catalytic activity. Even though some multifunctional TMN catalysts show multiple active sites for catalytic reactions, their activity is not ideal. Therefore, developing multifunctional and high-performance catalysts is an important research direction. For example, in water decomposition, TMN catalysts with high HER/OER activity should be developed; in fuel cells or metal air batteries, TMN catalysts with high ORR/OER activity should be developed.

Fourthly, although metal nitrides have high stability in electrocatalysis, they are not stable under extreme pH conditions. Most TMN catalysts can only exhibit high stability in the environments where the pH is not too low or too high, so it is an important research topic to study how TMN catalysts can maintain high stability for a long time under extreme conditions. In addition, some TMN catalysts have high activity and stability under acidic or alkaline conditions, but the catalysts that can maintain good catalytic activity and stability under both acidic and alkaline conditions are currently rarely



reported. Therefore, developing TMN catalysts that have high catalytic activity and stability in acid and alkaline systems is another important research direction.

Fifthly, the choice of substrate is particularly important. The synergistic effect between substrate and metal nitride can provide more active sites, enhance conductivity and stability. However, an unsuitable substrate will cause the opposite effect and even make the catalyst fall off from the substrate, so it is very important to select a suitable substrate. At present, the widely used substrates include metal substrates such as nickel foam and carbon materials. Improving the substrate to obtain higher activity catalysts is an effective method.

Finally, more catalyst modification methods should be tried. The activity of a single-metal nitride is still quite different from that of a noble metal catalyst. Modification is an effective way to improve catalytic performance. Heteroatom doping can optimize the electronic structure of metal nitrides to improve activity, conductivity and stability. In addition to doping with other metals shown above, non-metallic atoms such as S, P, or noble metal atoms could be tried to obtain more advanced metal nitrides. The utilization of active sites can also be improved by adjusting the morphology of metal nitrides.

## Conflicts of interest

There is no conflict to declare.

## Acknowledgements

This work was supported by the Sichuan Science and Technology Program (2023NSFSC0086) and the Fundamental Research Funds for the Central Universities (YJ2021156).

## References

- (a) C. Wang and D. Astruc, *Chem. Soc. Rev.*, 2021, **50**, 3437–3484; (b) J. Wei, X. Chen and S. Li, *J. Electrochem.*, 2022, **28**, 2214012; (c) W. Xie and M. Shao, *J. Electrochem.*, 2022, **28**, 22014008.
- (a) K. Zhang, W. Mai, J. Li, G. Li, L. Tian and W. Hu, *ACS Appl. Nano Mater.*, 2019, **2**, 5931–5941; (b) Z. Wan, C. Wang and X. Kang, *J. Electrochem.*, 2022, **28**, 2214005.
- K. R. Yoon, C.-K. Hwang, S.-H. Kim, J.-W. Jung, J. E. Chae, J. Kim, K. A. Lee, A. Lim, S.-H. Cho, J. P. Singh, J. M. Kim, K. Shin, B. M. Moon, H. S. Park, H.-J. Kim, K. H. Chae, H. C. Ham, I.-D. Kim and J. Y. Kim, *ACS Nano*, 2021, **15**, 11218–11230.
- B. Guo, J. Sun, X. Hu, Y. Wang, Y. Sun, R. Hu, L. Yu, H. Zhao and J. Zhu, *ACS Appl. Nano Mater.*, 2019, **2**, 40–47.
- D. J. Ham and J. S. Lee, *Energies*, 2009, **2**, 873–899.
- W.-F. Chen, K. Sasaki, C. Ma, A. I. Frenkel, N. Marinkovic, J. T. Muckerman, Y. Zhu and R. R. Adzic, *Angew. Chem., Int. Ed.*, 2012, **51**, 6131–6135.
- J. G. Chen, *Chem. Rev.*, 1996, **96**, 1477–1498.
- J. E. Houston, G. E. Laramore and R. L. Park, *Science*, 1974, **185**, 258–260.
- J. Luo, X. Tian, J. Zeng, Y. Li, H. Song and S. Liao, *ACS Catal.*, 2016, **6**, 6165–6174.
- L. Johansson, *Surf. Sci. Rep.*, 1995, **21**, 177–250.
- R. Niewa and F. J. DiSalvo, *Chem. Mater.*, 1998, **10**, 2733–2752.
- Y. Fan, S. Ida, A. Staykov, T. Akbay, H. Hagiwara, J. Matsuda, K. Kaneko and T. Ishihara, *Small*, 2017, **13**, 1700099.
- B. Zhang, C. Xiao, S. Xie, J. Liang, X. Chen and Y. Tang, *Chem. Mater.*, 2016, **28**, 6934–6941.
- S. Tang, Z. Zhang, J. Xiang, X. Yang, X. Shen and F. Song, *Front. Chem.*, 2022, **10**, 1073175.
- R. Qin, P. Wang, C. Lin, F. Cao, J. Zhang, L. Chen and S. Mu, *Acta Phys.-Chim. Sin.*, 2021, **37**, 2009099.
- Z. Chen, Y. Ha, Y. Liu, H. Wang, H. Yang, H. Xu, Y. Li and R. Wu, *ACS Appl. Mater. Interfaces*, 2018, **10**, 7134–7144.
- H. Shin, H. I. Kim, D. Y. Chung, J. M. Yoo, S. Weon, W. Choi and Y. E. Sung, *ACS Catal.*, 2016, **6**, 3914–3920.
- W. Li, C.-Y. Cao, C.-Q. Chen, Y. Zhao, W.-G. Song and L. Jiang, *Chem. Commun.*, 2011, **47**, 3619–3621.
- B. Wang, M. Lu, D. Chen, Q. Zhang, W. Wang, Y. Kang and Z. Fang, *J. Mater. Chem. A*, 2021, **9**, 13562–13569.
- J. Yu, H. Guo, W. Feng, X. Guo, Y. Zhu, T. Thomas, C. Jiang, S. Liu and M. Yang, *Dalton Trans.*, 2022, **51**, 7127–7134.
- Y. Ma, L. Xiong, Y. Lu, W. Zhu, H. Zhao, Y. Yang, L. Mao and L. Yang, *Front. Chem.*, 2021, **9**, 638216.
- H. Wu and W. Chen, *J. Am. Chem. Soc.*, 2011, **133**, 15236–15239.
- R. Deshmukh and U. Schubert, *J. Mater. Chem.*, 2011, **21**, 18534–18536.
- Y. Yuan, J. Wang, S. Adimi, H. Shen, T. Thomas, R. Ma, J. P. Attfield and M. Yang, *Nat. Mater.*, 2020, **19**, 282–286.
- J. Choi and E. G. Gillan, *Inorg. Chem.*, 2009, **48**, 4470–4477.
- H. Xu, D. Wang, P. Yang, A. Liu, R. Li, Y. Li, L. Xiao, X. Ren, J. Zhang and M. An, *J. Mater. Chem. A*, 2020, **8**, 23187–23201.
- J. Li, M. Chen and D. A. Cullen, *Nat. Catal.*, 2018, **1**, 935–945.
- X. Ding, S. Yin, K. An, L. Luo, N. Shi, Y. Qiang, S. Pasupathi, B. G. Pollet and P. K. Shen, *J. Mater. Chem. A*, 2015, **3**, 4462–4469.
- S. Luca and B. Matteo, *Materials*, 2021, **14**, 7590–7590.
- R. Fix, R. G. Gordon and D. M. Hoffman, *Chem. Mater.*, 1991, **3**, 1138–1148.
- H. Wang, E. J. S. Rosado, S. H. Tsang, J. Lin, M. Zhu, G. Mallick, Z. Liu and E. H. T. Teo, *Adv. Funct. Mater.*, 2019, **29**, 1902663.
- Y. Han, X. Yue, Y. Jin, X. Huang and P. K. Shen, *J. Mater. Chem. A*, 2016, **4**, 3673–3677.
- B. K. Dana and P. W. Bohn, *Analyst*, 2010, **135**, 902–907.
- Z. Liang, C. Qu, W. Guo, R. Zou and Q. Xu, *Adv. Mater.*, 2018, **30**, 1870276.

- 35 R. Yadagiri, B. K. Kumar, P. Bhavesh and S. Eringathodi, *J. Solid State Chem.*, 2015, **223**, 23–31.
- 36 Y. Hu, C. Li, S. Xi, Z. Deng, X. Liu, A. K. Cheetham and J. Wang, *Adv. Sci.*, 2021, **8**, 2003212.
- 37 F. Wang, H. Zhao, Y. Ma, Y. Yang, B. Li, Y. Cui, Z. Guo and L. Wang, *J. Energy Chem.*, 2020, **50**, 52–62.
- 38 Y. Wang, X. Cui, J. Zhao, G. Jia, L. Gu, Q. Zhang, L. Meng, Z. Shi, L. Zheng, C. Wang, Z. Zhang and W. Zheng, *ACS Catal.*, 2019, **9**, 336–344.
- 39 Y. Zhu, G. Chen, X. Xu, G. Yang, M. Liu and Z. Shao, *ACS Catal.*, 2017, **7**, 3540–3547.
- 40 J.-T. Ren, K. Yuan, K. Wu, L. Zhou and Y.-W. Zhang, *Inorg. Chem. Front.*, 2019, **6**, 366–375.
- 41 Z. Cai, J. Dai, W. Li, K. B. Tan, Z. Huang, G. Zhan, J. Huang and Q. Li, *ACS Catal.*, 2020, **10**, 13275–13289.
- 42 Y. Sun, Z. Dong, D. Zhang, Z. Zeng, H. Zhao, B. An, J. Xu and X. Wang, *Sens. Actuators, B*, 2021, **326**, 128791.
- 43 D. Yu, Q. Shao, Q. Song, J. Cui, Y. Zhang, B. Wu, L. Ge, Y. Wang, Y. Zhang, Y. Qin, R. Vajtai, P. M. Ajayan, H. Wang, T. Xu and Y. Wu, *Nat. Commun.*, 2020, **11**, 927.
- 44 D. Raja, P. Pradip, B. Rahul and P. Pankaj, *Nanoscale*, 2012, **4**, 591–599.
- 45 Y. Zhu, G. Chen, Y. Zhong, W. Zhou and Z. Shao, *Adv. Sci.*, 2018, **5**, 1700603.
- 46 S. Wang, D. Antonio, X. Yu, J. Zhang, A. L. Cornelius, D. He and Y. Zhao, *Sci. Rep.*, 2015, **5**, 13733.
- 47 D. Kerdoud, F. Benkafada, N. Boussouf and C. Benhamideche, *Ann. Chim.-Sci. Mat.*, 2022, **46**, 103–108.
- 48 X. Xie, H. Sun, Z. Xu, M. Wang, X. Chen and J. Han, *New J. Chem.*, 2019, **43**, 14714–14719.
- 49 H. Zhao, M. Lei, X. Chen and W. Tang, *J. Mater. Chem.*, 2006, **16**, 4407–4412.
- 50 N. Han, P. Liu, J. Jiang, L. Ai, Z. Shao and S. Liu, *J. Mater. Chem. A*, 2018, **6**, 19912–19933.
- 51 P. Zheng, J. Zhao, J. Zheng, G. Ma and Z. Zhu, *J. Mater. Chem. A*, 2012, **22**, 12116–12120.
- 52 N. Gordillo, R. G. Arrabal, P. D. Chao, J. R. Ares, I. J. Ferrer, F. Yndurain and F. A. López, *Thin Solid Films*, 2013, **531**, 588–591.
- 53 T. Kou, M. Chen, F. Wu, T. J. Smart, S. Wang, Y. Wu, Y. Zhang, S. Li, S. Lall, Z. Zhang, Y.-S. Liu, J. Guo, G. Wang, Y. Ping and Y. Li, *Nat. Commun.*, 2020, **11**, 590.
- 54 Y. Guo, T. Park, J. W. Yi, J. Henzie, J. Kim, Z. Wang, B. Jiang, Y. Bando, Y. Sugahara, J. Tang and Y. Yamauchi, *Adv. Mater.*, 2019, **31**, 1807134.
- 55 S. Aparna, P. A. Mary, N. Ravi, G. Kannan, G. T. Selvi, J. George, M. Muthumareeswaran, P. Saravanan, A. Abdullah, K. S. Young, V. L. Quyet, S. P. Loke, J. S. Kwan and G. A. Nirmala, *Sci. Rep.*, 2022, **12**, 2004–2004.
- 56 C. Shi, A. M. Zhu, X. F. Yang and C. T. Au, *Appl. Catal., A*, 2004, **276**, 223–230.
- 57 S. Adimi, W. Qi, T. Thomas, R. Gebauer, M. Yang and S. Ruan, *Mater. Adv.*, 2021, **2**, 3394–3404.
- 58 I. Milošev, H.-H. Strehblow, M. Gaberšček and B. Navinšek, *Surf. Interface Anal.*, 1996, **24**, 448–458.
- 59 J. Jia, M. Zhai, J. Lv, B. Zhao, H. Du and J. Zhu, *ACS Appl. Mater. Interfaces*, 2018, **10**, 30400–30408.
- 60 L. Trotochaud, S. L. Young, J. K. Ranney and S. W. Boettcher, *J. Am. Chem. Soc.*, 2014, **136**, 6744–6753.
- 61 H. Liang, A. N. Gandi, D. H. Anjum, X. Wang, U. Schwingenschlögl and H. N. Alsharee, *Nano Lett.*, 2016, **16**, 7718–7725.
- 62 Y. Sun, L. Wang, O. Guselnikova, O. Semyonov, J. Fraser, Y. Zhou, N. Lopez and A. Y. Ganin, *J. Mater. Chem. A*, 2022, **10**, 855–861.
- 63 Y. Yuan, S. Adimi, T. Thomas, J. Wang, H. Guo, J. Chen, J. P. Attfield, F. J. DiSalvo and M. Yang, *Innovation*, 2021, **2**, 100096.
- 64 R. Zhang, J. Huang, G. Chen, W. Chen, C. Song, C. Li and K. Ostrikov, *Appl. Catal., B*, 2019, **254**, 414–423.
- 65 J. Li, Y. Wang, C. Liu, S. Li, Y. Wang, L. Dong, Z. Dai, Y. Li and Y. Lan, *Nat. Commun.*, 2016, **7**, 11204.
- 66 Y. Zhu, G. Chen, X. Xu, G. Yang and M. Liu, *ACS Catal.*, 2017, **7**, 3540–3547.
- 67 R. Ma, Y. Zhou, Y. Chen, P. Li, Q. Liu and J. Wang, *Angew. Chem., Int. Ed.*, 2015, **54**, 14723–14727.
- 68 L. Wang, Y. Li, X. Yin, Y. Wang, A. Song, Z. Ma, X. Qin and G. Shao, *ACS Sustainable Chem. Eng.*, 2017, **5**, 7993–8003.
- 69 A. P. Murthy, D. Govindarajan, J. Theerthagiri, J. Madhavan and K. Parasuraman, *Electrochim. Acta*, 2018, **283**, 1525–1533.
- 70 P. Zhou, D. Xing, Y. Liu, Z. Wang, P. Wang, Z. Zheng, X. Qin, X. Zhang, Y. Dai and B. Huang, *J. Mater. Chem. A*, 2019, **7**, 5513–5521.
- 71 M. Zhuang, X. Ou, Y. Dou, L. Zhang, Q. Zhang, R. Wu, Y. Ding, M. Shao and Z. Luo, *Nano Lett.*, 2016, **16**, 4691–4698.
- 72 R. Tong, M. Xu, H. Huang, C. Zhang, Y. Ma, X. Wang, X. Hu, Y. Qu, S. Wang and H. Pan, *ACS Appl. Energy Mater.*, 2022, **5**, 440–448.
- 73 P. J. McHugh, A. D. Stergiou and M. D. Symes, *Adv. Energy Mater.*, 2020, **10**, 2002453.
- 74 S. B. Lalvani and P. Rajagopal, *J. Electrochem. Soc.*, 2019, **139**, 1.
- 75 G. Stefan, A. Jens, E. Stephan and K. Helge, *J. Chem. Phys.*, 2010, **132**, 154104.
- 76 K. Xu, P. Chen, X. Li, Y. Tong, H. Ding, X. Wu, W. Chu, Z. Peng, C. Wu and Y. Xie, *J. Am. Chem. Soc.*, 2015, **137**, 4119–4125.
- 77 O. Mabayoje, A. Shoola, B. R. Wygant and C. B. Mullins, *ACS Energy Lett.*, 2016, **1**, 195–201.
- 78 K. Kawashima, R. A. M. Montes, H. Li, K. Shin, C. L. Cao, K. M. Vo, Y. J. Son, B. R. Wygant, A. Chunangad, D. H. Youn, G. Henkelman, V. H. R. Sánchez and C. B. Mullins, *Mater. Adv.*, 2021, **2**, 2299–2309.
- 79 L. Trotochaud, S. L. Young, J. K. Ranney and S. W. Boettcher, *J. Am. Chem. Soc.*, 2014, **136**, 6744–6753.
- 80 C. C. L. McCrory, S. Jung, J. C. Peters and T. F. Jaramillo, *J. Am. Chem. Soc.*, 2013, **135**, 16977–16987.
- 81 T. Reier, M. Oezaslan and P. Strasser, *ACS Catal.*, 2012, **2**, 1765–1772.

- 82 B. M. Tackett, W. Sheng, S. Kattel, S. Yao, B. Yan, K. A. Kuttiyil, Q. Wu and J. G. Chen, *ACS Catal.*, 2018, **8**, 2615–2621.
- 83 L. An, J. Feng, Y. Zhang, Y.-Q. Zhao, R. Si, G.-C. Wang, F. Cheng, P. Xi and S. Sun, *Nano Energy*, 2019, **57**, 644–652.
- 84 T. Liu, M. Li, X. Bo and M. Zhou, *ACS Sustainable Chem. Eng.*, 2018, **6**, 11457–11465.
- 85 Z.-H. Xue, H. Su, Q.-Y. Yu, B. Zhang, H.-H. Wang, X.-H. Li and J.-S. Che, *Adv. Energy Mater.*, 2017, **7**, 1602355.
- 86 M. Wu, G. Zhang, Y. Hu, J. Wang, T. Sun, T. Regier, J. Qiao and S. Sun, *Carbon Energy*, 2021, **3**, 176–187.
- 87 Y. Wu, Y. Liu, B. Liu, W. Jiang, T. Zhou, H. Li, M. Shang, J. Lang, C. Liu and G. Che, *ACS Appl. Nano Mater.*, 2022, **5**, 7714–7722.
- 88 J. Zhang, W. He, H. B. Aiyappa, T. Quast, S. Dieckhöfer, D. Öhl, J. R. C. Junqueira and Y.-T. Chen, *Adv. Mater. Interfaces*, 2021, **8**, 2100041.
- 89 Y. Wang, C. Xie, D. Liu, X. Huang, J. Huo and S. Wang, *ACS Appl. Mater. Interfaces*, 2016, **8**, 18652–18657.
- 90 S. Liang, M. Jing, E. Pervaiz, H. Guo, T. Thomas, W. Song, J. Xu, A. Saad, J. Wang, H. Shen, J. Liu and M. Yang, *ACS Appl. Mater. Interfaces*, 2020, **12**, 41464–41470.
- 91 J. Zhang, X. Zhao, L. Du, Y. Li, L. Zhang, S. Liao, J. B. Goodenough and Z. Cui, *Nano Lett.*, 2019, **19**, 7457–7463.
- 92 B. He, C. Dong, L. Yang, L. Ge and H. Chen, *J. Solid State Chem.*, 2011, **184**, 1939–1945.
- 93 X. L. Tian, J. M. Luo, H. X. Nan, Z. Y. Fu, J. H. Zeng and S. J. Liao, *J. Mater. Chem. A*, 2015, **3**, 16801–16809.
- 94 M. E. Kreider, A. Gallo, S. Back, Y. Liu, S. Siahrostami, D. Nordlund, R. Sinclair, J. K. Nørskov, L. A. King and T. F. Jaramillo, *ACS Appl. Mater. Interfaces*, 2019, **11**, 26863–26871.
- 95 T. Huang, S. Mao, G. Zhou, Z. Wen, X. Huang, S. Cib and J. Chen, *Nanoscale*, 2014, **6**, 9608–9613.
- 96 M. E. Kreider, M. B. Stevens, Y. Liu, A. M. Patel, M. J. Statt, B. M. Gibbons, A. Gallo, M. B. Naim, A. Mehta, R. C. Davis, A. V. Ievlev, J. K. Nørskov, R. Sinclair, L. A. King and T. F. Jaramillo, *Chem. Mater.*, 2020, **32**, 2946–2960.
- 97 D. A. Miura, C. R. Navarro, Y. Masubuchi and M. Higuchi, *Angew. Chem., Int. Ed.*, 2016, **55**, 7963–7967.
- 98 Y. Matsumoto, H. Yoneyama and H. Tamura, *J. Electroanal. Chem.*, 1977, **79**, 319–326.
- 99 Li An, W. Huang, N. Zhang, X. Chen and D. Xia, *J. Mater. Chem. A*, 2014, **2**, 62–65.
- 100 K. E. Fritz, Y. Yan and J. Suntivich, *Nano Res.*, 2019, **12**, 2307–2312.
- 101 B. Cao, J. C. Neuefeind, R. R. Adzic and P. G. Khalifah, *ACS Appl. Nano Mater.*, 2015, **54**, 2128–2136.
- 102 X. L. Tian, L. Wang, B. Chi, Y. Xu, S. Zaman, K. Qi, H. Liu, S. Liao and B. Y. Xia, *ACS Catal.*, 2018, **8**, 8970–8975.
- 103 M. Zhou, H.-L. Wang and S. Guo, *Chem. Soc. Rev.*, 2016, **45**, 1273–1307.
- 104 Q. Wang, L. Shang, R. Shi, X. Zhang, G. I. N. Waterhouse, L. Z. Wu, C. H. Tung and T. Zhang, *Nano Energy*, 2017, **40**, 382–389.
- 105 Y. Dong, Y. Deng, J. Zeng, H. Song and S. Liao, *J. Mater. Chem. A*, 2017, **5**, 5829–5837.
- 106 Y. Ma, W. Chen, Z. Jiang, X. Tian, X. WangGuo, G. Chend and Z.-J. Jiang, *J. Mater. Chem. A*, 2022, **10**, 12616–12631.
- 107 R. Zeng, Y. Yang, X. Feng, H. Li, L. M. Gibbs and F. J. Disalvo, *Sci. Adv.*, 2022, **8**, 1584.
- 108 M. S. Balogun, Y. C. Huang, W. T. Qiu, H. Yang, H. B. Ji and Y. X. Tong, *Mater. Today*, 2017, **20**, 425–451.
- 109 J. Luo, X. Qiao, J. Jin, X. Tian, H. Fan, D. Yu, W. Wang, S. Liao, N. Yuf and Y. Deng, *J. Mater. Chem. A*, 2020, **8**, 8575–8585.
- 110 R. Jasinski, *Nature*, 1964, **201**, 1212–1213.
- 111 J. Chen, X. Wei, J. Zhang, Y. Luo, Y. Chen, G. Wang and R. Wang, *Ind. Eng. Chem. Res.*, 2019, **58**, 2741–2748.
- 112 J. Jia, Z. Chen, Y. Liu, Y. Li and J. Zhao, *ACS Appl. Mater. Interfaces*, 2020, **12**, 54517–54523.
- 113 X. Zhao and Y. Pei, *J. Phys. Chem. C*, 2021, **125**, 12541–12550.
- 114 M. Mazzucato, L. Gavioli, V. Balzano, E. Berretti, G. A. Rizzi, D. Badocco, P. Pastore, A. Zitolo and C. Durante, *ACS Appl. Mater. Interfaces*, 2022, **14**, 54635–54648.
- 115 B. Liu, B. He, H.-Q. Peng, Y. Zhao, Y. Cheng, J. Xia, J. Shen, T.-W. Ng, X. Meng, C.-S. Lee and W. Zhang, *Adv. Sci.*, 2018, **5**, 1800406.
- 116 J. Su, Y. Yang, G. Xia, J. Chen, P. Jiang and Q. Chen, *Nat. Commun.*, 2017, **8**, 14969.
- 117 H. Jin, X. Liu, A. Vasileff, Y. Jiao, Y. Zhao, Y. Zheng and S.-Z. Qiao, *ACS Nano*, 2018, **12**, 12761–12769.
- 118 M. Zhou, Q. Weng, Z. I. Popov, Y. Yang, L. Yu. Antipina, P. B. Sorokin, X. Wang, Y. Bando and D. Golberg, *ACS Nano*, 2018, **12**, 4148–4155.
- 119 S. H. Kwag, Y. S. Lee, J. Lee, D. I. Jeong, S. B. Kwon, J. H. Yoo, S. Woo, B. S. Lim, W. K. Park, M.-J. Kim, J. H. Kim, B. Lim, B. K. Kang, W. S. Yang and D. H. Yoon, *ACS Appl. Energy Mater.*, 2019, **2**, 8502–8510.
- 120 Y. He, X. Liu, A. Yan, H. Wan, G. Chen, J. Pan, N. Zhang, T. Qiu, R. Ma and G. Qiu, *ACS Sustainable Chem. Eng.*, 2019, **7**, 19612–19620.
- 121 G. S. Shanker and S. Ogale, *ACS Appl. Energy Mater.*, 2021, **4**, 2165–2173.
- 122 W. Wang, L. Liu, W. C. Leng, L. L. Cui and Y. Gong, *Inorg. Chem.*, 2021, **60**, 12136–12150.
- 123 J. Hao, W. Yang, Z. Peng, C. Zhang, Z. Huang and W. Shi, *ACS Catal.*, 2017, **7**, 4214–4220.
- 124 H. Huang, C. Yu, X. Han, S. Li, S. Cui, C. Zhao, H. Huang and J. Qiu, *Ind. Eng. Chem. Res.*, 2017, **56**, 14245–14251.
- 125 Y. Wang, S. Hao, X. Liu, Q. Wang, Z. Su, L. Lei and X. Zhang, *ACS Appl. Mater. Interfaces*, 2020, **12**, 37006–37012.
- 126 T. Liu, Y. Tian, M. Li, Z. Su, J. Bai, C. Ma, X. Bo, W. Guan and M. Zhou, *Electrochim. Acta*, 2019, **323**, 134684.



- 127 C. Zhang, B. Ma, Y. Zhou and C. Wang, *J. Electroanal. Chem.*, 2020, **865**, 114142.
- 128 J. M. Jaksic, N. V. Krstajić, B. N. Grgur and M. M. Jakšić, *Surf. Eng.*, 1984, **23**, 667–681.
- 129 O. Y. Bisen, R. Nandan and K. K. Nanda, *ACS Omega*, 2020, **5**, 32852–32860.
- 130 H. Xu, Y. Jack, R. Ge, J. Zhang, Y. Li, M. Zhu, L. Dai, S. Li and W. Li, *J. Energy Chem.*, 2022, **71**, 234–265.
- 131 J. Han, H. Bao, J.-Q. Wang, L. Zheng, S. Sun, Z. L. Wang and C. Sun, *Appl. Catal., B*, 2021, **280**, 119411.
- 132 L. Li, G. Chen and X. Chen, *e-Polymers*, 2022, **22**, 883–897.
- 133 P. D. Sutrisna, N. Prasetya, N. F. Himma and I. G. Wenten, *J. Chem. Technol. Biotechnol.*, 2020, **95**, 2767–2774.
- 134 H. S. Gujral, G. Singh, A. V. Baskar, X. Guan, X. Geng, A. V. Kotkondawar, S. Rayalu, P. Kumar, A. Karakoti and A. Vinu, *Sci. Technol. Adv. Mater.*, 2022, **23**, 76–119.
- 135 K. Wang, X. Wang, Z. Li, B. Yang, M. Ling, X. Gao, J. Lu, Q. Shi, L. Lei, G. Wu and Y. Hou, *Nano Energy*, 2020, **77**, 10512.
- 136 Y. Ray, P. Eugenie, J. Denis, Q. Zhi and D. Abdoulaye, *J. Electrochem. Soc.*, 2022, **169**, 063513.
- 137 D. Gao, J. Zhang, T. Wang, W. Xiao, K. Tao, D. Xuea and J. Ding, *J. Mater. Chem. A*, 2016, **4**, 17363–17369.
- 138 D. Han, J. Cai, Y. Xie, Y. Wu, S. Niu, Y. Zang, H. Pan, W. Qu, G. Wang and Y. Qian, *Adv. Energy Sustainability Res.*, 2022, **3**, 2100219.
- 139 Y. Zhang, B. Ouyang, J. Xu, G. Jia, S. Chen, R. S. Rawat and H. J. Fan, *Angew. Chem., Int. Ed.*, 2016, **55**, 8670–8674.
- 140 Y. Yang, R. Zeng, Y. Xiong, F. J. DiSalvo and H. D. Abruna, *J. Am. Chem. Soc.*, 2019, **141**, 19241–19245.
- 141 S. Sanati, A. Morsali and H. García, *Energy Environ. Sci.*, 2022, **15**, 3119–3151.
- 142 B. Wu, H. Meng, D. M. Morales, F. Zeng, J. Zhu, B. Wang, M. Risch, Z. J. Xu and T. Petit, *Adv. Funct. Mater.*, 2022, **32**, 2204137.
- 143 Q. Zhi, R. Jiang, W. Liu, T. Sun, K. Wang and J. Jiang, *Nano Res.*, 2022, **15**, 1803–1808.
- 144 S. Ding, Q. Chen, S. Chen, Y. Tian and J. Zhang, *Chin. Chem. Lett.*, 2023, DOI: [10.1016/j.cclet.2023.108232](https://doi.org/10.1016/j.cclet.2023.108232).